Journal of Geophysical Research: Solid Earth

RESEARCH ARTICLE
10.1029/2018JB015900

Key Points:
- Ultrasonic velocity and permeability correlate systematically with the intensity of open and sealed microfractures
- Sealed microfractures significantly increase velocity and pose a challenge for deriving crack porosity using effective-medium models
- The estimated change in velocity associated with sealing matches seismological observations of velocity recovery following earthquakes

Correspondence to:
M. Rempe,
marieke.rempe@rub.de

Citation:
Rempe, M., Mitchell, T. M., Renner, J., Smith, S. A. F., Bistacchi, A., & Di Toro, G. (2018). The relationship between microfracture damage and the physical properties of fault-related rocks: The Gole Larghe Fault Zone, Italian Southern Alps. *Journal of Geophysical Research: Solid Earth*, *123*, 7661–7687. https://doi.org/10.1029/2018JB015900

Received 3 APR 2018
Accepted 28 AUG 2018
Accepted article online 6 SEP 2018
Published online 27 SEP 2018

The Relationship Between Microfracture Damage and the Physical Properties of Fault-Related Rocks: The Gole Larghe Fault Zone, Italian Southern Alps

Marieke Rempe[1], Thomas M. Mitchell[2], Jörg Renner[1], Steven A. F. Smith[3], Andrea Bistacchi[4], and Giulio Di Toro[5,6]

[1]Ruhr-Universität Bochum, Bochum, Germany, [2]Rock and Ice Physics Laboratory & SeismoLab, Department of Earth Sciences, University College London, London, UK, [3]University of Otago, Dunedin, New Zealand, [4]Dipartimento di Scienze dell'Ambiente e della Terra, Università degli Studi di Milano Bicocca, Milano, Italy, [5]Dipartimento di Geoscienze, Università degli Studi di Padova, Padua, Italy, [6]Istituto Nazionale di Geofisica e Vulcanologia, Rome, Italy

Abstract Although geological, seismological, and geophysical evidence indicates that fracture damage and physical properties of fault-related rocks are intimately linked, their relationships remain poorly constrained. Here we correlate quantitative observations of microfracture damage within the exhumed Gole Larghe Fault Zone (Italian Southern Alps) with ultrasonic wave velocities and permeabilities measured on samples collected along a 1.5-km-long transect across the fault zone. Ultrasonic velocity and permeability correlate systematically with the measured microfracture intensity. In the center of the fault zone where microfractures were pervasively sealed, *P* wave velocities are the highest and permeability is relatively low. However, neither the crack porosity nor the permeability derived by modeling the velocity data using an effective-medium approach correlates well with the microstructural and permeability measurements, respectively. The applied model does not account for sealing of microfractures but assumes that all variations in elastic properties are due to microfracturing. Yet we find that sealing of microfractures affects velocities significantly in the more extensively altered samples. Based on the derived relationships between microfracture damage, elastic and hydraulic properties, and mineralization history, we (i) assess to what extent wave velocities can serve as a proxy for damage structure and (ii) use results on the present-day physical and microstructural properties to derive information about possible postseismic recovery processes. Our estimates of velocity changes associated with sealing of microfractures quantitatively agree with seismological observations of velocity recovery following earthquakes, which suggests that the recovery is at least in part due to the sealing of microfractures.

1. Introduction

The structure of fault zones exerts a significant influence on the mechanical and hydraulic properties of the crust due to the intimate relationships between fracture damage and the physical properties of fault-related rocks (e.g., Townend & Zoback, 2000). Constraining the relationships between fault damage and physical properties is important for the interpretation of seismic data and assessment of the feedback between damage, rupture mechanics, and fluid flow (Stierman, 1984).

Fault zones are often characterized by a fault core that is surrounded by a damage zone in which the intensity of fracture damage decreases with distance from the fault core (e.g., Caine et al., 1996; Chester et al., 1993; Lee et al., 2001; Wibberley & Shimamoto, 2003). More complex fault zones consist of a heterogeneous damage zone structure with multiple fault strands (e.g., Childs et al., 2009; Faulkner et al., 2003), as is the case for the Gole Larghe Fault Zone (GLFZ) in Italy (Smith et al., 2013). The damage structure of fault zones is related to their permeability structure (Caine et al., 1996; Knipe, 1992). When a fault core consists of low-permeability gouge, it may hinder fluid pressure diffusion and thus maintain low effective pressure that can lead to low fault strength (Faulkner et al., 2003). Highly fractured permeable rocks will instead enhance fluid flow in the core (Mitchell & Faulkner, 2008, 2012). Under hydrothermal conditions, high permeability and associated fluid flow lead to progressive sealing of fractures due to mineral precipitation and thus to a decrease of permeability with time. This process has been replicated in experiments (Morrow et al., 2001; Tenthorey & Fitz Gerald, 2006) and inferred from geophysical surveys of fault zones following earthquakes (e.g., Li et al., 2004). It is important to understand the feedbacks between fracture damage, fluid flow, and associated sealing of fractures by mineral precipitation, and the elastic properties of fault-related rocks. The interplay between these parameters exerts a strong influence on strength recovery in fault zones and thus the

mechanics of future earthquakes. For example, a high degree of sealing and an associated strengthening of the fault appear to be responsible for long earthquake recurrence intervals and high stress drops in the following rupture (Houston, 1990; Kanamori & Allen, 1986). Relations between different physical properties were previously established from micromechanical modeling exploiting the common dependence of properties on a specific microstructural parameter (Berryman & Milton, 1988). However, as elastic and hydraulic properties share only some governing microstructural parameters, their cross-property connection was found to be qualitative at most (e.g., Sevostianov & Kachanov, 2009). Also, different properties might be governed by different modes of a distribution of microstructural elements; for example, permeability is potentially controlled by the narrowest fracture in a network, while seismic velocity depends on a mean aperture.

Geophysical studies have suggested that seismic wave velocities may be used as a proxy for the intensity of fracture damage within fault zones (e.g., Jeppson et al., 2010; Li et al., 2004). The possibility to remotely characterize a fault zone with measurements of seismic velocity is particularly attractive because seismic velocity is relatively easy and fast to measure from the surface, while the determination of permeability and characterization of damage require drilling into the area of interest. For example, seismological studies, which have the advantage not only to probe the presently exposed fault area but also to penetrate larger depths and thus currently active fault areas, indicate that regions of decreased wave velocity and high V_p/V_s ratio correlate with highly fractured regions within fault cores (Li et al., 1990, 2004; Mooney & Ginzburg, 1986; Zhao et al., 1996). Such low-velocity zones have been detected in a number of active faults, including in the San Andreas Fault Observatory at Depth by seismic reflection imaging (Li & Malin, 2008) and borehole geophysical logging at a depth of 3–4 km (Jeppson et al., 2010). Combining these observations with the composition of drill cuttings from San Andreas Fault Observatory at Depth (Bradbury et al., 2007), the relatively low velocity zone was related to a combination of (i) fracture damage, (ii) alteration of rocks associated with an increase in the abundance of clay minerals that have low intrinsic seismic velocity, and (iii) locally high porosities (Jeppson et al., 2010). In light of micromechanical modeling, the high V_p/V_s ratio detected in fault zones likely indicates the presence of pressurized fluids (O'Connell & Budiansky, 1974), as these will compensate for the decrease in *P* wave velocities due to damage but leaving *S* wave velocities largely unaffected. The inferred presence of fluids causing the high V_p/V_s ratio inside fault zones also suggests increased permeability in fault zones compared to wall rocks (Byerlee, 1990; Rice, 1992).

Few studies have quantified the relationships between fracture damage, seismic velocity, and permeability across the entire width of a single large fault zone. In this study, existing data on the structure of the GLFZ (Smith et al., 2013) are combined with new measurements of microfracture intensity and orientation. These results are correlated with laboratory measurements of ultrasonic wave velocities and permeabilities of samples collected from a 1.5-km-long transect across the fault zone. Using these data, we test the applicability of micromechanical models for the relationships between elastic properties and degree of damage, enabling us to evaluate their significance and transferability to other fault zones. Of the current models based on effective-medium theory that link elastic properties and damage (Budiansky & O'Connell, 1976; Kachanov, 1993; Kuster & Toksöz, 1974; Zimmerman, 1984), we employ the noninteraction approach by Kachanov (1993) to model crack porosity. We use modeled crack porosity values to estimate permeability and thus explore the link between the elastic and hydraulic properties of the samples. We establish a work flow for modeling crack porosity, aspect ratio, and permeability from measurements of seismic velocity on natural rocks and test the applicability of the model relations to the fault-related rocks from the Gole Larghe Fault Zone.

2. Geologic Setting

The GLFZ is an exhumed dextral transpressive strike-slip fault zone cutting the Adamello batholith in the Italian Southern Alps (Figure 1; Di Toro & Pennacchioni, 2005). The Adamello batholith is located between the Tonale Line to the north and the Southern Giudicarie Line to the southeast, both of which are segments of the Periadriatic Lineament, the major tectonic structure that separates the Eastern and the Southern Alps (Dal Piaz et al., 2003). The Adamello batholith comprises several plutons that were progressively emplaced from c. 42 to 29 Ma at pressures of 250–350 MPa, corresponding to depths of 9–11 km. The GLFZ is hosted in tonalites of the Val d'Avio-Val di Genova pluton intruded at c. 34–32 Ma (Figure 1; Del Moro et al., 1983). Following pluton emplacement and crystallization, seismic faulting occurred at c. 30 Ma at temperatures of 250–300 °C and a depth of c. 8 km (Pennacchioni et al., 2006).

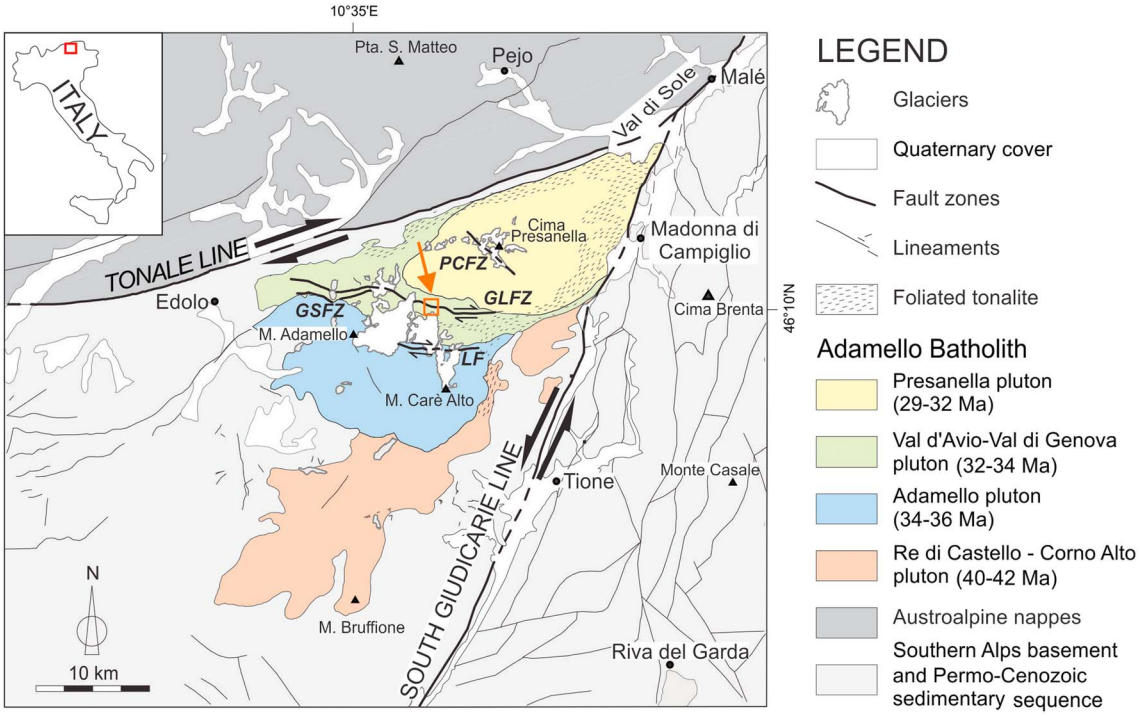

Figure 1. Geologic setting of the Gole Larghe Fault Zone (GLFZ) in the Adamello batholith (after Mittempergher et al., 2009). The Adamello batholith is composed of several plutons, which were emplaced subsequently (see legend). Outcrop location along the GLFZ, which is shown in detail in Figure 2, is marked with orange rectangular and arrow.

The GLFZ has a length of c. 20 km and a thickness of c. 500–600 m (Figure 2). This thickness corresponds to the width of the zone that contains fault and fracture densities above regional *background* values (Smith et al., 2013). Brittle damage within the GLFZ includes (i) cataclastic faults that often reactivated preexisting cooling joints in the tonalite, (ii) pseudotachylyte-bearing faults, and (iii) pervasively developed networks of macro- and microfractures related to (i) and (ii). The damage structure and mechanics of faulting within the GLFZ were previously investigated in detail (Di Toro et al., 2005, 2009; Di Toro & Pennacchioni, 2004, 2005). Subsequently, Smith et al. (2013) investigated fault-perpendicular transects (Figure 2a) and documented a broadly symmetric pattern of macrofracture and microfracture intensities (Figure 3a). Based on their analyses, Smith et al. (2013) subdivided the GLFZ into several zones with different damage characteristics. Macro- and microfracture intensities are lowest in the tonalitic wall rocks outside the fault zone (Figure 3a). Inside the fault zone, fracture intensity increases systematically toward a central zone that is bordered on each side by thick (c. 2 m) cataclastic faults (Figures 2a and 3a). The elevated microfracture intensity extends up to 50 m beyond the central zone (Figure 3a).

A further defining feature of the GLFZ is a distinct fluid-alteration zone, characterized by pervasive filling of fractures at all scales by epidote, K-feldspar, and chlorite and by a diffuse alteration of biotite to chlorite and sericitization of plagioclase (Mittempergher et al., 2014; Smith et al., 2013). This alteration gives outcrops and samples within the alteration zone a characteristic green color (Figure 3b). Because we consider only the microscale damage of samples in this paper, we distinguish three zones: (1) fluid-alteration zone, (2) damage zone, and (3) wall rock. Our terminology slightly deviates from that of Smith et al. (2013) who based their identification of the central zone mainly on the macrofracture intensity.

3. Methods

3.1. Sample Collection and Microfracture Analysis

Forty-six oriented samples were collected along transects running across the entire width of the Gole Larghe Fault Zone (Figure 2a; see also Smith et al., 2013). The selection of samples avoided major cataclasite- and

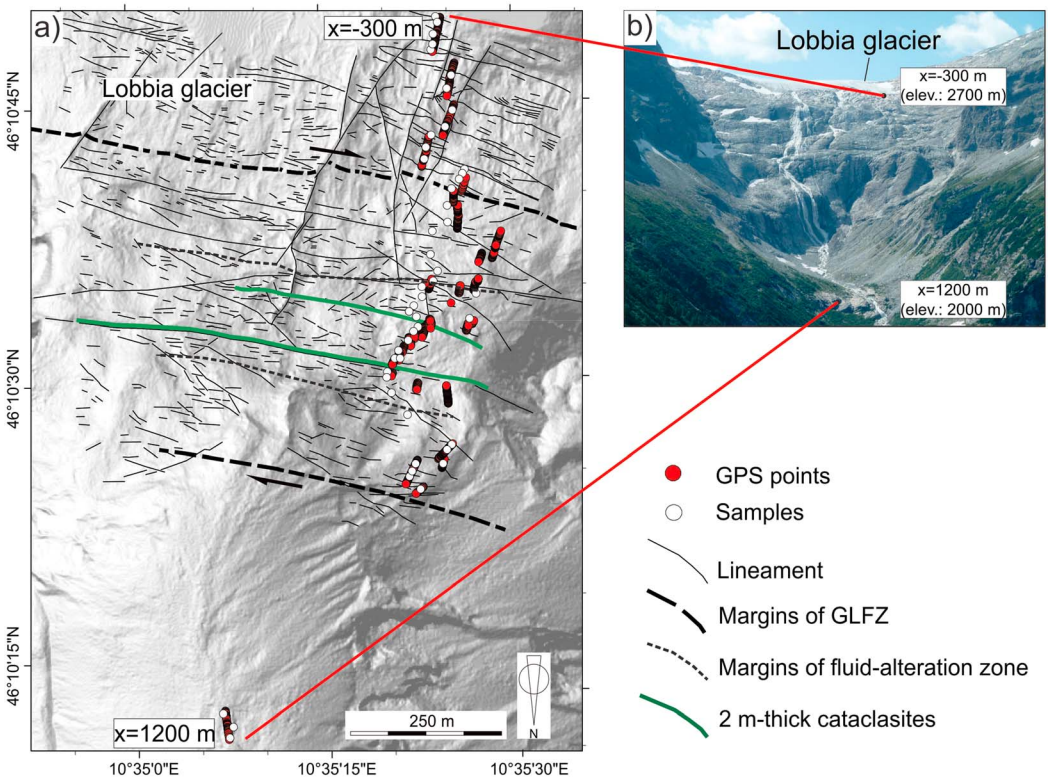

Figure 2. Sample locations. (a) Map of the field area modified from Smith et al. (2013) showing the location of the GPS points (red symbols) at which intersections of macrofractures with GPS line transects were detected. We use x values to refer to the location along the transects such that they start at $x = -300$ m at an elevation of 2,700 m in the south and end at $x = 1{,}200$ m at an elevation of 2,000 m in the north (e.g., Figure 3). A total of 46 oriented samples (white symbols) were taken along the line transects. The southern and northern margins of the fault zone are shown as black dashed lines and the locations of the 2-m-thick cataclasites within the fluid-alteration zone as green lines. (b) Photograph of the Lobbia Glacier area (looking south), where the GLFZ is exposed along our 1,500 m-long transect.

pseudotachylyte-bearing fault strands, such that samples include only the large-scale variation of accumulated microfracture density in the tonalite. The samples thus likely represent the damage that would be *seen* by the large wavelengths employed by in situ seismic studies, because the cataclasite- and pseudotachylyte-bearing fault strands represent just a subordinate fraction of the total fault volume.

For the microstructure analysis, oriented thin sections were prepared that represent the true horizontal plane (Figure 4). Ultrasonic velocity measurements were conducted on oriented cubic samples cut from each hand specimen with horizontal, strike-parallel, and strike-perpendicular surfaces. In some cases, several cubic samples were cut from one hand specimen, yielding a total of 83 samples. Oriented cylindrical cores with length and diameter of up to 75 and 30 mm, respectively, were prepared for permeability measurements in fault-parallel, fault-perpendicular, and vertical directions.

Macrofractures in the GLFZ dip mainly to the south at angles of c. 60° (Smith et al., 2013). A close match between the orientation of micro- and macrofractures has been found in many previous studies (Anders et al., 2014, and references therein). Thus, microfractures are also expected to show dominant dip angles of c. 60° and the orientations of microfracture traces obtained from horizontal thin sections are likely not significantly biased by the microfracture dip (see also Appendix A1 for an estimation of the microfracture orientation bias).

Smith et al. (2013) determined the number of intersections of microfractures, P_{10} (following the terminology of Mauldon & Dershowitz, 2000), with a randomly oriented test line in quartz grains (because fracture orientation is little affected by crystallographic characteristics of this mineral in comparison to the other common phases in the tonalite, feldspar, and biotite). We complemented these by measurements of the total fracture

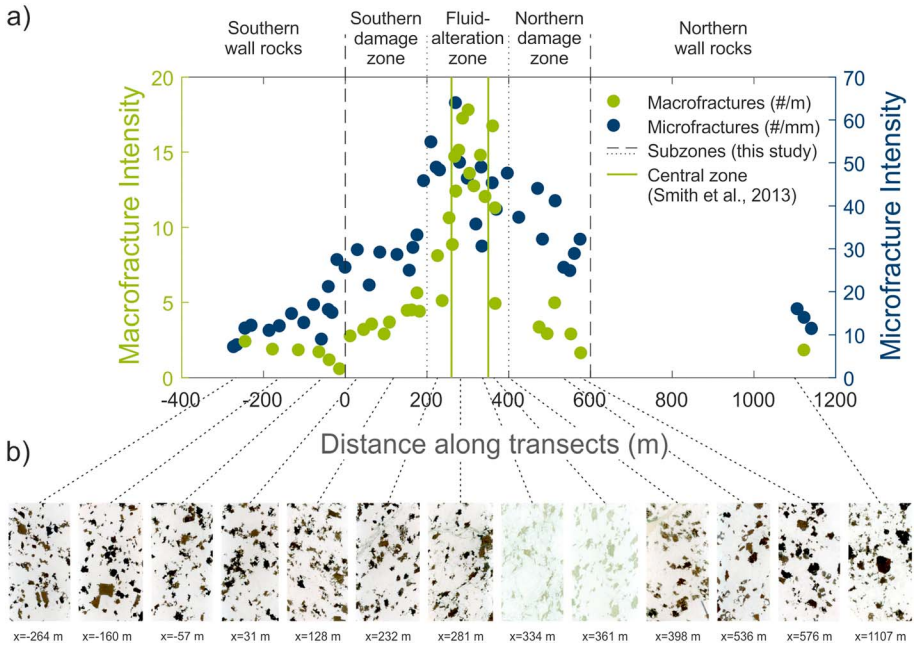

Figure 3. Macroscale and microscale damage structure of the Gole Larghe fault (modified after Smith et al. (2013). (a) Macrofracture intensity (green symbols) includes joints, faults, fractures, and cataclastic bands whose location along the line transects was determined using differential GPS. Here we classify the symmetric structure by three subzones, that is, wall rocks, damage zones, and fluid-alteration zone, the latter including the *central zone* bounded by two 2-m-thick cataclastic bands (green lines) identified by Smith et al. (2013) based on the macroscale damage. Total microfracture intensity (blue symbols) includes sealed and open microfractures determined with the point-intersection method. (b) Thin-section scans of selected samples showing the change to green coloration of the rocks from the fluid-alteration zone due to progressive transformation of black biotite to green chlorite. A magmatic foliation as found in other parts of the Adamello batholith is not observable.

length per area, P_{21} (compare Griffith et al., 2010). Fractures and grain boundaries were manually traced in digital images covering a thin section area of c. 2.5 mm^2. Each fracture trace consists of discrete, straight segments that connect nodes, such that the total fracture length is calculated from the sum of the length of segments. The orientation of the fracture traces was determined individually for every fracture segment; that is, long fractures composed of many segments contribute with a highly weighted value to orientation statistics. We classified microfractures either as *open* (i.e., not containing a mineral fill), as *fluid inclusion planes* (FIPs), or as *sealed* (i.e., containing a mineral fill), while Smith et al. (2013) included fluid-inclusion planes and sealed fractures in one group. A description of the procedure by which the uncertainty of the microfracture intensity was estimated is given in Appendix A1.

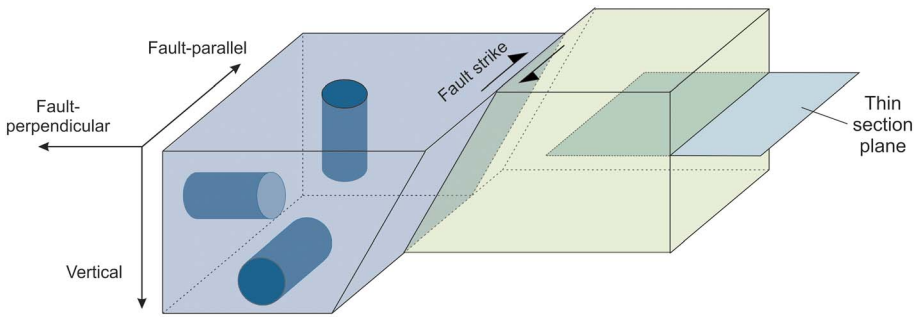

Figure 4. Orientation of samples and associated terminology of directions reflecting the fault strike. Sample cubes have three orthogonal surfaces oriented horizontally and parallel and perpendicular to the fault strike. The fault plane has a dip angle of c. 60°. Thin sections are cut in the horizontal plane. The long axes of the cylindrical samples used for permeability measurements are oriented parallel and perpendicular to the fault strike and in vertical direction.

Table 1
Sample Volume, Bulk Density, and Connected Porosity

Zone	Sample name	Distance from fault margin (m)	V (cm^3)	ρ (kg/m^3)		φ_{conn} (%)	
Southern wall rocks	465	−272	4.2	2,683	±6.4	0.62	±0.005
	526	−244	8.3	2,687	±3	0.74	±0.003
	567	−229	3.0	2,694	±9	1.08	±0.007
	836	−185	2.4	2,719	±11	1.18	±0.008
	876	−160	2.2	2,684	±12	1.01	±0.008
	916	−130	2.8	2,599	±9	1.04	±0.008
	964	−100	13.1	2,703	±2	0.83	±0.002
	302	−76	3.0	2,634	±9	1.05	±0.006
	258	−57	0.8	2,709	±36	1.10	±0.020
	236	−40	6.1	2,582	±4	0.76	±0.004
	200A	−40	3.1	2,688	±9	0.81	±0.007
	200B	−31	2.6	2,627	±10	0.68	±0.007
	200C	−19	4.6	2,692	±6	0.73	±0.004
Southern damage zone	Ste01	31	3.9	2,716	±7	0.98	±0.005
	Ste02	60	1.8	2,673	±14	1.31	±0.012
	Ste03	86	1.2	2,686	±22	1.20	±0.024
	Ste04	128	3.6	2,607	±7	1.11	±0.006
	Ste05	158	5.7	2,546	±4	0.81	±0.004
	Ste06	177	5.8	2,683	±5	0.70	±0.004
	Ste07	193	4.3	2,702	±6	0.89	±0.005
Fluid-alteration zone	Ste08	211	2.6	2,654	±10	0.63	±0.007
	Ste36	224	2.6	2,654	±10		
	Ste09	232	2.3	2,702	±12	0.78	±0.007
	Ste12	271	9.4	2,709	±3	0.61	±0.002
	Ste13	281	3.9	2,666	±7	0.66	±0.005
	Ste14	300	0.8	2,730	±33	0.74	±0.013
	Ste16	336	1.1	2,689	±25	1.01	±0.015
	Ste15	321	1.4	2,688	±19	0.74	±0.011
	Ste17	334	3.5	2,538	±7	1.36	±0.007
	Ste19	371	1.8	2,644	±15	0.86	±0.010
	Ste20	398	8.2	2,697	±3	0.53	±0.003
	Ste21	426	4.4	2,702	±5	0.86	±0.005
Northern damage zone	Ste30	472	7.5	2,706	±4	1.12	±0.004
	Ste31	484	7.6	2,724	±4	0.93	±0.004
	Ste28	515	4.1	2,662	±7	1.53	±0.008
	Ste27	536	1.6	2,716	±17	1.01	±0.019
	Ste26	551	6.8	2,722	±4	1.86	±0.005
	Ste25	562	3.7	2,716	±7	1.29	±0.009
	Ste29	576	2.6	2,614	±10	1.29	±0.012
Wall rocks	Ste24	1,107	3.4	2,726	±8	1.34	±0.009
	Ste22	1,142	2.4	2,731	±11	0.93	±0.012

3.2. Laboratory Measurements of Physical Properties

3.2.1. Bulk Density, Porosity, and Ultrasonic Velocity Measurements

Measurements of bulk density, porosity, and ultrasonic velocity were performed on the prepared cubic samples ranging from 10^2 to 10^3 cm^3 in volume (Table 1). The bulk density of the samples was determined using Archimedes' method and the connected porosity from imbibition with water. Laboratory measurements of ultrasonic *P* and *S* wave velocities were performed on oven-dry and saturated samples using broadband sensors with a central frequency of 1 MHz, a pulse generator (rectangular signal, central frequency 1 MHz), and a digital storage oscilloscope. The samples were unconfined, but the sensors were pressed on the samples with an axial stress of about 0.06 to 0.3 MPa (depending on the cross-sectional area of the sample) in the direction of wave propagation. Contact gel was applied to the sensors to ensure reproducible coupling on the rough sample surface. Velocities were measured in three directions (parallel and perpendicular to fault strike and in vertical direction, Figure 4). Thus, up to three *P* wave and six *S* wave velocities (due to the polarization of *S* waves) were measured for each sample. The first breaks were usually picked with an uncertainty of <0.4 μs for *P* waves and c. 0.75 μs for *S* waves, resulting in velocity errors generally $\leq 10\%$, although problems

Table 2
Permeability Measurement Conditions

Sample name[a]	Distance (m)	Method	$P_{eff,max}$ (MPa)[b]
465_pa	−272	Pore pressure oscillation	10
465_v	−272	Pore pressure oscillation	60
964_pa	−100	Pore pressure oscillation	60
964_pe	−100	Pore pressure oscillation	190
964_v	−100	Pore pressure oscillation	90
200C_pa	−19	Pore pressure oscillation	90
200C_pe	−19	Pore pressure oscillation	90
Ste02_pa	60	Steady state flow	60
Ste04_pa	128	Pore pressure oscillation	60
Ste04_pe	128	Pore pressure oscillation	90
Ste04_v	128	Pore pressure oscillation	90
Ste06_pa	177	Steady state flow	30
Ste17_pa	334	Pore pressure oscillation	60
Ste17_pe	334	Pore pressure oscillation	60
Ste18_pa	361	Pore pressure oscillation	60
Ste18_pe	361	Pore pressure oscillation	10
Ste28_pa	515	Steady state flow	90
Ste29_pa	576	Steady state flow	90
Ste24_pa	1107	Steady state flow	60

[a]Suffix _pa, _pe, and _v denote direction of permeability measurement (fault-parallel and fault-perpendicular and vertical, respectively). [b]Effective pressure corresponds to unweighted difference between confining and pore fluid pressure.

in uniquely identifying the first onset of the *S* wave might in some cases cause a larger error. Based on the difference in *P* wave velocity in the three orientations, samples were characterized as isotropic (velocity differences within experimental uncertainty), as transversely isotropic (velocity in one directions deviates from the other two by more than the uncertainty), or as orthotropic (velocities in all directions deviate from each other by more than the uncertainty). The symmetry classification thus depends on the picking error of first arrivals of *P* waves. For our picking error of 0.4 μs, 70% of the samples are classified as isotropic.

3.2.2. Permeability Measurements

Permeability measurements relied on the pore pressure oscillation method (Bennion & Goss, 1971; Bernabé et al., 2006; Fischer, 1992; Stewart et al., 1961) for the majority of samples, but some samples were tested with the steady state flow method (Table 2). The experimental setup consisted of a pressure vessel in which a jacketed sample was subjected to hydrostatic pressure using oil as the confining medium. The pore pressure system, composed of an upstream and a downstream reservoir, was filled with distilled water. Confining pressure and upstream pore pressure were servohydraulically controlled.

Permeability was generally determined at nominal effective pressures, here defined as difference between confining and pore fluid pressure, of 10, 30, 60, and 90 MPa. (Effective pressures of up to 190 MPa were applied in some cases, Table 2.) For measurements using the pore pressure oscillation method, a sinusoidal oscillation of the upstream pore pressure with amplitudes and periods ranging from 1 to 4 MPa and 50 to 5,000 s, respectively, was superimposed on the nominal pore pressure of 10 MPa. The phase shift and amplitude ratio of the response in the downstream reservoir were determined by Fourier analysis of the pressure records, from which permeability was derived using the analytical solution of the 1-D diffusion equation for harmonic flow through a homogeneous, isotropic, porous medium (Bernabé et al., 2006; Fischer, 1992; Kranz et al., 1990).

We represent the pressure dependence of permeability by the permeability modulus $K_k = -\partial p_c/\partial \ln k|_{p_f}$. Furthermore, the permeability measurements were extrapolated to constrain the permeability at zero pressure, k_0, to allow for a comparison to the measurements of ultrasonic velocity and porosity performed at ambient pressure (section 3.2.1). We fit the linear relation $\ln k = \ln k_0 - \Delta p/K_k$ to the data valid for a constant permeability modulus (following David et al., 1994, and Rice, 1992) by singular-value decomposition that provides uncertainties of the fit parameters (Sotin & Poirier, 1984).

3.3. Micromechanical Modeling

3.3.1. Crack Porosity and Aspect Ratio

The equivalent crack porosity was estimated from measured ultrasonic velocities using the effective-medium approach by Kachanov (1993). The model quantifies the effect of cracks on the compliance of a rock that—when crack free—is isotropic with Young's modulus E_0 and shear modulus G_0. The effective Young's and shear moduli (E_c and G_c) of a cracked body containing randomly oriented, identical penny-shaped cracks are then given by (Benson et al., 2006; Kachanov, 1993; Schubnel et al., 2006)

$$\frac{E_0}{E_c} = 1 + \left\{1 + \frac{3}{5}\left[\left(1 - \frac{\nu_0}{2}\right)\frac{\delta}{1+\delta} - 1\right]\right\}\frac{16\left(1-\nu_0^2\right)}{9(1-\nu_0/2)}\psi \tag{1}$$

and

$$\frac{G_0}{G_c} = 1 + \left\{1 + \frac{2}{5}\left[\left(1 - \frac{\nu_0}{2}\right)\frac{\delta}{1+\delta} - 1\right]\right\}\frac{16(1-\nu_0)}{9(1-\nu_0/2)}\psi. \tag{2}$$

Here $\nu_0 = E_0/(2G_0) - 1$ is the Poisson's ratio of the crack-free body and δ is the fluid coupling parameter that quantifies the impact of a crack-filling fluid on the elastic properties. The dimensionless crack density is defined as

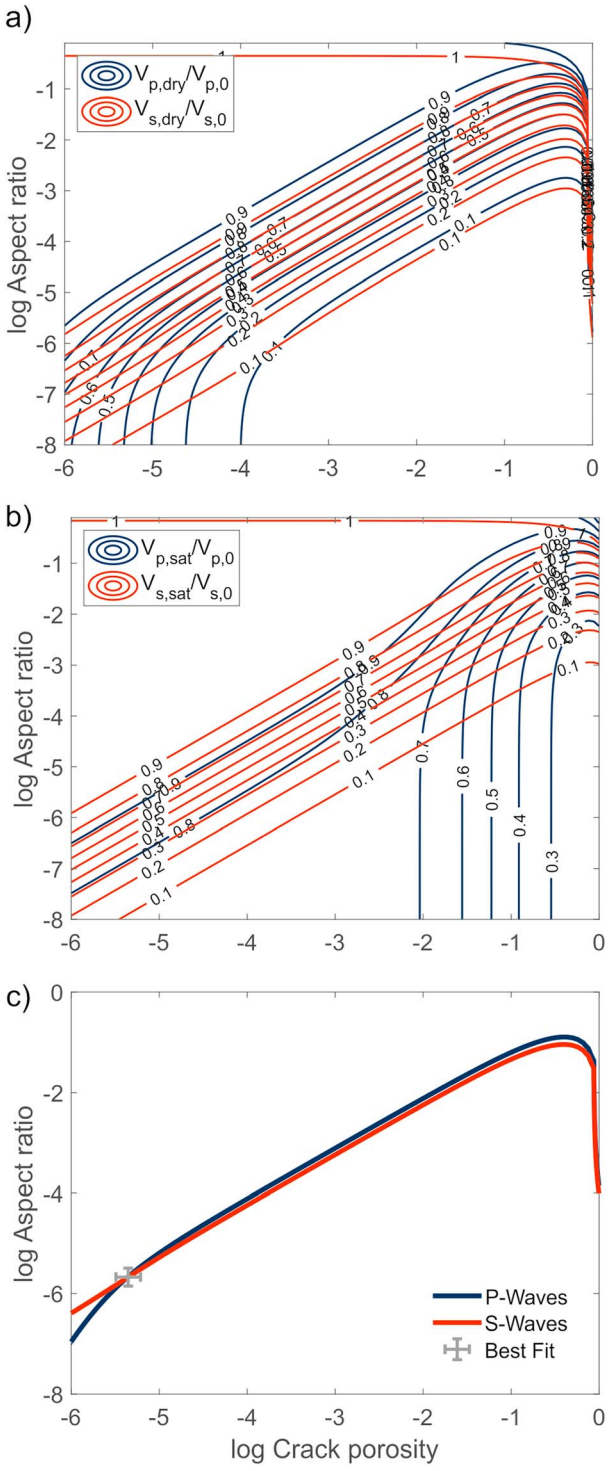

Figure 5. Dependence of *P* and *S* wave velocities on crack porosity and aspect ratio. (a) Dry case. (b) Saturated case. (c) Example of the isolines for normalized *P* and *S* wave velocities. The intersection of the two bold lines yields the best fit for crack porosity and aspect ratio.

$$\psi \equiv \frac{Nc^3}{V_b} \tag{3}$$

and relates to equivalent crack porosity ϕ_c according to

$$\phi_c = \frac{N\pi c^2 w}{V_b} = \pi\psi\frac{w}{c} = \pi\psi\zeta, \tag{4}$$

with the number of cracks per unit volume N/V_b, the crack radius c, and the crack aperture w, such that $\zeta = w/c \leq 1$ is the crack's aspect ratio. The bulk density $\rho_c = (1 - \phi_c)\rho_0 + \phi_c\rho_f$ of the cracked medium is related to crack porosity by

$$\frac{\rho_c}{\rho_0} = 1 - \left(1 - \frac{\rho_f}{\rho_0}\right)\phi_c \simeq \begin{cases} 1 - \phi_c \text{ for dry rocks with } \rho_f \to 0 \\ 1 - \frac{2}{3}\phi_c \text{ for water-saturated rocks} \end{cases}. \tag{5}$$

where we introduced the bulk density of the crack-free rock, ρ_0, and the density of the fluid filling the cracks, ρ_f.

As $v_S(\phi_c, \zeta)/v_{S,0} = \sqrt{G_c\rho_0/G_0\rho_c}$ and the fluid coupling parameter results to

$$\delta = \frac{9}{16\left(1 - \nu_0^2\right)}\frac{E_0}{K_f}\zeta \tag{6}$$

for penny-shaped cracks when assuming that all change in the crack volume is due to aperture variations (Kachanov, 1993; Schubnel et al., 2006), the normalized effective shear velocity is given by

$$\frac{v_{S,\mathrm{eff}}(\phi_c, \zeta)}{v_{S,0}} = \sqrt{\frac{1}{1 - \left(1 - \frac{\rho_f}{\rho_0}\right)\phi_c}\frac{1}{1 + \left[1 - \frac{9\nu_0 E_0\zeta + 32K_f\left(1-\nu_0^2\right)}{45E_0\zeta + 80K_f\left(1-\nu_0^2\right)}\right]\frac{16(1-\nu_0)}{9\left(1-\frac{\nu_0}{2}\right)}\frac{\phi_c}{\pi\zeta}}}. \tag{7}$$

An expression similar to (7) holds for the normalized *P* wave velocity:

$$\frac{v_{P,\mathrm{eff}}(\phi_c, \zeta)}{v_{P,0}} = \frac{v_{S,\mathrm{dry}}(\phi_c, \zeta)}{v_{S,0}}\sqrt{\frac{4G_c - E_c}{3G_c - E_c}\frac{3G_0 - E_0}{4G_0 - E_0}}. \tag{8}$$

We determined equivalent crack porosity and aspect ratio from fitting equations (7) and (8) to *P* and *S* wave velocities measured for dry and saturated samples (Figure 5). The uncertainty of crack porosity and aspect ratio was determined by propagating the velocity errors.

3.3.2. Permeability and Its Pressure Dependence

The permeability of a rock depends on the geometrical characteristics of the present pores and fractures and on their interconnection. In a medium containing randomly distributed, identical penny-shaped cracks the permeability is given by

$$k_0 = \frac{4\pi^2}{15}\frac{N}{V_b}f\zeta^3c^5 = \frac{4\pi}{15}\phi_c f w^2, \tag{9}$$

(Dienes, 1982; Guéguen & Schubnel, 2003), where f denotes the fraction of interconnected cracks with regard to the total number of cracks per unit volume N/V_b. The fraction of interconnected cracks f can be determined from percolation theory, which treats the problem of the probability of cracks to intersect and form a hydraulically interconnected network,

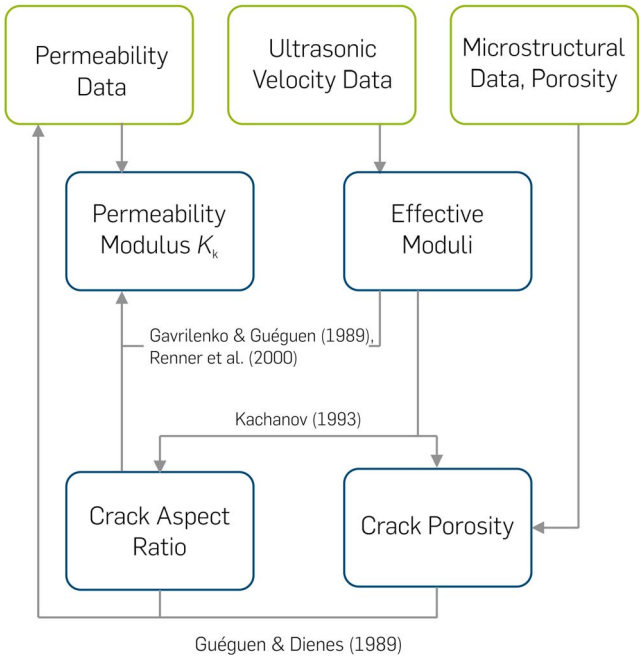

Figure 6. Schematic diagram illustrating the relation of the measured, derived, and modeled parameters. Measurement values are shown in green boxes, derived and modeled values in blue ones. Citations refer to models previously used to interrelate the parameters.

$$f \simeq \begin{cases} 0 & \text{for } \frac{\pi}{4}\frac{\phi_c}{\zeta} \leq \frac{1}{3} \\ \frac{9}{4}(p-p_c)^2 = \frac{9}{4}\left(\frac{\pi}{4}\frac{\phi_c}{\zeta} - \frac{1}{3}\right)^2 & \text{for } \frac{1}{3} < \frac{\pi}{4}\frac{\phi_c}{\zeta} < 1 \\ 1 & \text{for } \frac{\pi}{4}\frac{\phi_c}{\zeta} > 1 \end{cases} \quad (10)$$

where p describes the probability of cracks to intersect and p_c represents the percolation threshold below which no flow occurs (Guéguen & Schubnel, 2003). According to equation (9), permeability k_0 is not only a function of the crack aspect ratio but also of an absolute length scale of the fracture geometry (length c or aperture w). The interconnectivity of fractures may also implicitly depend on their geometry since relatively wide or short cracks will lower the fraction of interconnected cracks. For the derivation of equation (10), it is assumed that fractures are arranged on a simple lattice and thus have four neighboring fractures (Dienes, 1982; Guéguen & Dienes, 1989). Using these relations, the permeability of our samples can be estimated from equivalent crack porosity as modeled from ultrasonic velocities (Figure 6).

A second link between crack density and permeability results from the pressure dependence of permeability (Figure 6). Assuming that all fractures contribute to flow and that their closure is purely elastic, a *dynamic permeability modulus*

$$K_{k,dyn} \equiv -\left.\frac{\partial \Delta p}{\partial \ln k}\right|_{p_f} \simeq \frac{\zeta E_0}{9(1-\nu_0^2)}, \quad (11)$$

(Gavrilenko & Guéguen, 1989; Renner et al., 2000) is gained from the ultrasound velocities and the modeled aspect ratio and may be compared to the experimentally determined $K_{k,static}$.

4. Results

4.1. Microfracture Intensity and Orientation

Thin section analysis revealed the presence of open and sealed microfractures and FIPs. The length of fractures ranges from submillimeter to centimeter scale; sealed fractures frequently have a relatively wide aperture (up to c. 120 μm) compared to open fractures, and FIPs are sometimes observed along cleavage planes (see Figure 8 of Smith et al., 2013). In the southern wall rocks, the traces of both FIPs and open microfractures mainly strike E-W, that is, parallel to the overall fault strike (Figure 7a). In a sample collected close to the border of the southern damage zone ($x = -76$ m), the orientation of a prominent fracture set is roughly NNE-SSW and close to fault perpendicular, with minor sets striking ESE-WNW and ENE-WSW (Figure 7a). This ESE-WNW orientation is consistent with the orientation of postmagmatic cooling joints (Pennacchioni et al., 2006). Within the southern damage zone, the most common orientation of FIPs and open microfractures is still E-W, but samples show a more widely distributed microfracture orientation (e.g., sample at $x = 1$ m) or a N-S striking microfracture set (e.g., samples at $x = 177$ m). In the fluid-alteration zone, a dominant microfracture orientation is not present; some samples show mainly E-W striking microfractures ($x = 281$ m), some roughly N-S striking ($x = 321$ m), others relatively random orientations ($x = 300$ m).

The P_{21} microfracture intensity generally increases from the southern wall rocks to the southern damage zone, but then, in contrast to the P_{10} values (shown in Figure 7a for comparison), decreases within the fluid-alteration zone to reach its lowest values in the northern wall rocks (Figure 7a). Most of the fractures (64%) determined with the length-per-area (P_{21}) method are classified as fluid-inclusion planes (FIPs; Figure 7b) except in the northern damage zone, where open fractures dominate (Figure 7b). Some samples from the damage and fluid-alteration zone show increased intensities of sealed fractures without a systematic trend.

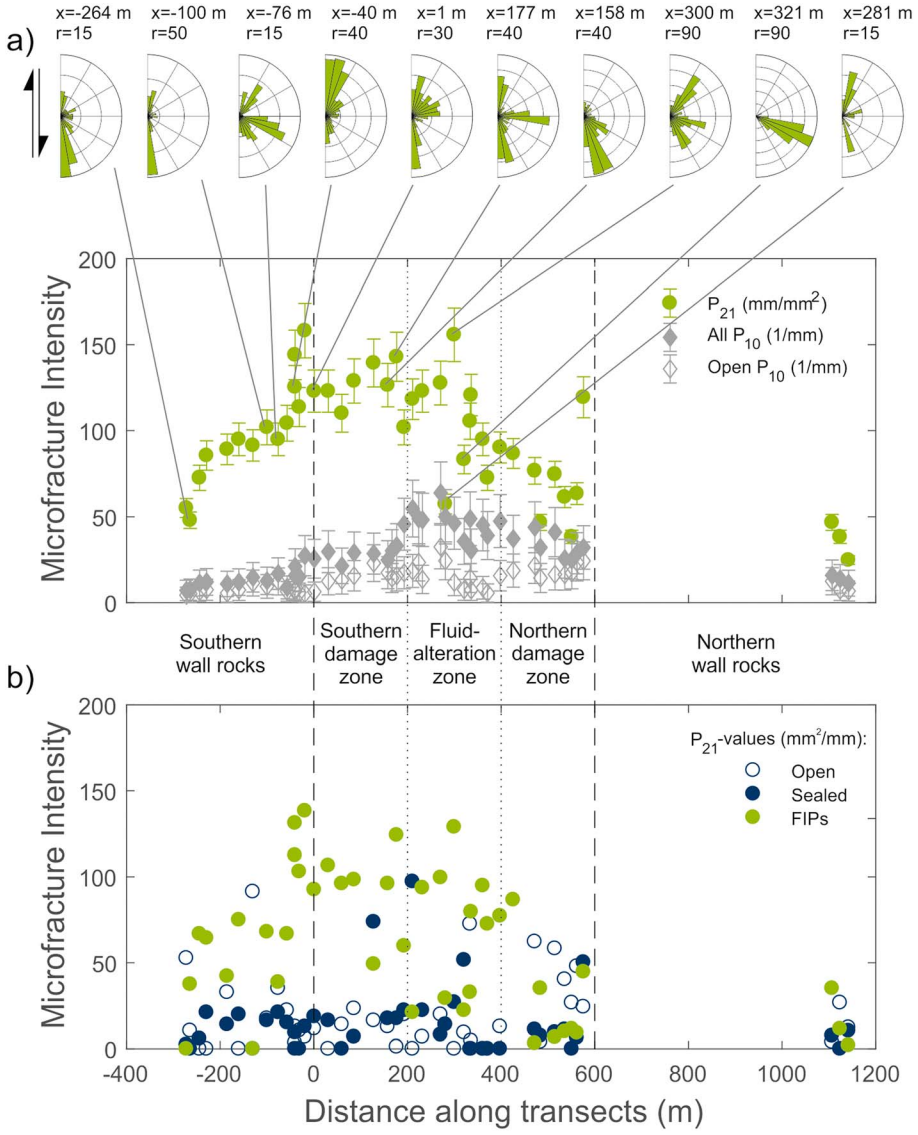

Figure 7. Variation of microfracture orientation and intensity across the fault zone. (a) Rose diagrams show orientation of fluid-inclusion planes (FIPs) for selected samples. The vertical edges of the rose diagrams correspond to E-W direction, that is, parallel to the fault strike. The radius, *r*, of the rose diagrams is written above each diagram and was adjusted to the total number of FIPs of that specific sample. Total microfracture intensity obtained from fracture tracing (mm/mm^2, green symbols) in comparison to fracture intensity obtained with the point-intersection method (1/mm, gray symbols; Smith et al., 2013). (b) Variation of P_{21} microfracture intensity for the three subdivisions, FIPs, sealed and open fractures.

4.2. Experimental Results

4.2.1. Bulk Density, Connected Porosity, and Ultrasonic Velocity

The bulk density derived by Archimedes' method (Table 1) does not show a dependence on location along the transects. In contrast, the connected porosity of the samples varies systematically across the fault zone (Figure 8a). Within the southern wall rocks, connected porosity increases from 0.6 to 1.2% toward the southern damage zone and then decreases to reach a minimum at the southern border of the fault zone (i.e., x = 0 m). In the southern damage zone, connected porosity increases again to values of up to c. 1.3%. In the fluid-alteration zone the connected porosity is generally low (c. 0.7%) with a few notable exceptions. The variation in connected porosity is relatively high in the northern damage zone, but porosity appears to generally increase toward the wall rocks north of the fault zone ($x > 1000$ m), where porosity is also quite high (0.9–1.4%).

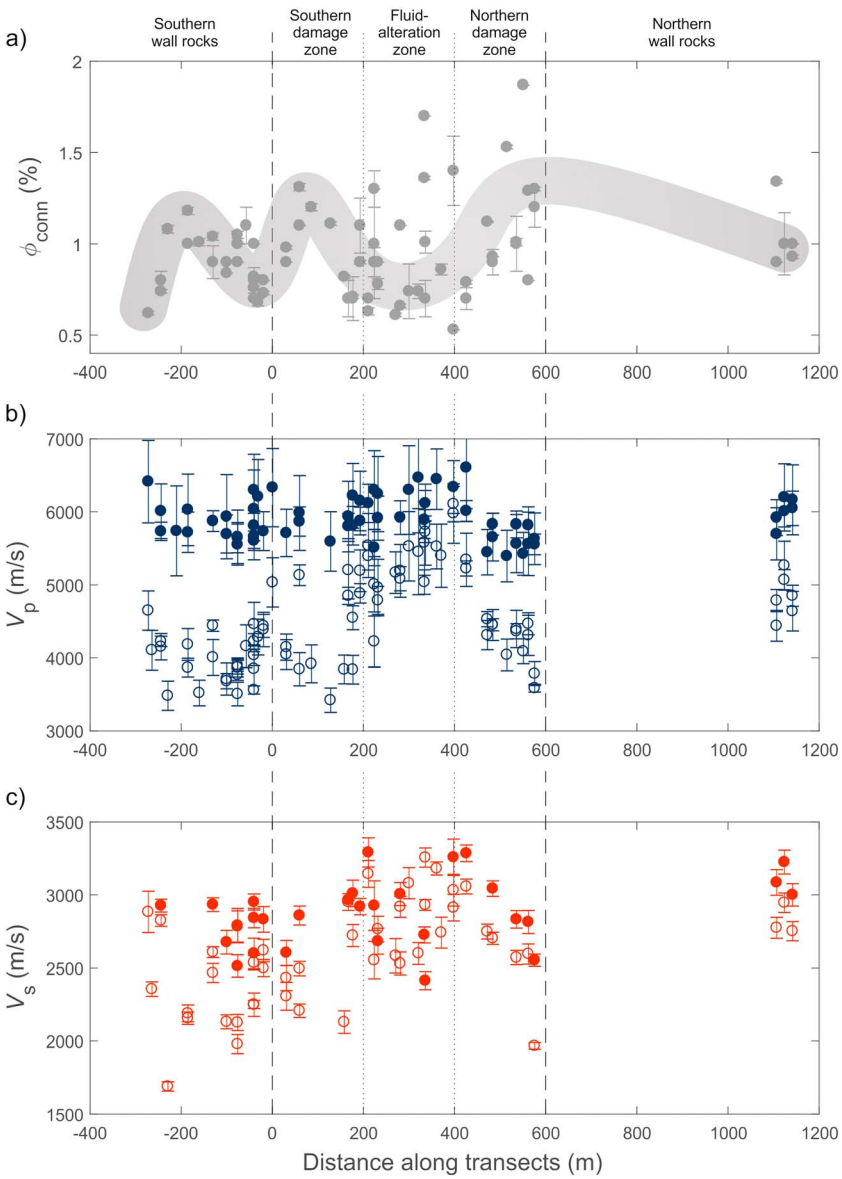

Figure 8. Connected porosity and ultrasonic wave velocities. (a) Connected porosity in %. Gray line highlights overall trend of porosity along transects. (b) *P* wave and (c) *S* wave velocities measured on dry (open symbols) and saturated (filled symbols) samples, averaged over the three orthogonal directions.

P wave velocities of dry samples from the northern wall rocks (c. 5,000 m/s; Figure 8b) are significantly higher than that from the southern wall rocks where fluctuations between c. 3,500 and c. 4,800 m/s occur. In contrast, the damage zone exhibits no asymmetry but velocities are similar in its northern and southern part (i.e., c. 4,000 m/s). In the fluid-alteration zone, *P* wave velocities reach values of c. 5,000–6,000 m/s, higher than anywhere else. In general, the *S* wave velocities show the same overall trends as the *P* wave velocities, albeit with less pronounced variations (Figure 8c).

Upon water saturation of samples, *P* wave velocity increases by c. 2,000–3,000 m/s in the southern wall rocks and the southern and northern damage zone, but only by c. 1,000 m/s in the fluid-alteration zone (Figure 8b). Overall, saturation diminishes the variability of *P* wave velocities across the fault zone and the contrast in *P* wave velocity between fluid-alteration zone and wall and damage zone rocks. The *S* wave velocities measured on samples from the wall rocks and southern and northern damage zone increase upon saturation,

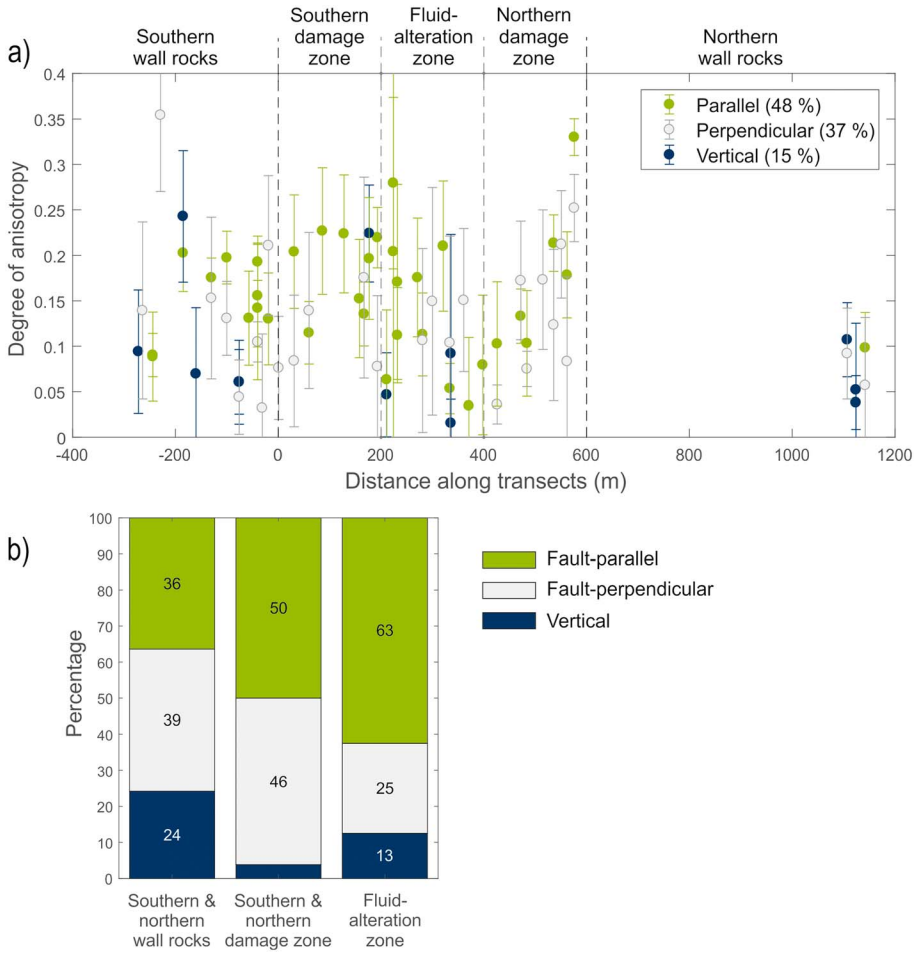

Figure 9. Anisotropy of the samples as deduced from the velocity measurements. (a) Variation of the degree of anisotropy, $(V_{p,max} - V_{p,min})/\overline{V_p}$, with location along the transects. The color coding corresponds to the direction of the slowest velocity as shown in legend. (b) The percentage of the direction of the slowest velocity, that is, fault-parallel, fault-perpendicular, or vertical, for the three subzones.

too, albeit to a smaller degree than the *P* wave velocities (Figure 8c), therefore yielding a higher average V_p/V_s ratio inside the fluid-alteration zone ($V_p/V_s \approx 2$) than outside ($V_p/V_s \approx 1.75$).

The degree of anisotropy, that is, the difference between highest and lowest velocity normalized by its average value, ranges from 0.02 to 0.35 and varies moderately with location across the fault zone (Figure 9a). For about half of the samples (48%), the lowest velocity is observed in the horizontal fault-parallel direction, while only 15% of the samples exhibit the lowest velocity in the vertical direction (Figure 9a). However, these values differ somewhat for the different subzones (Figure 9b): In the wall rocks, the lowest velocity is detected with a similar frequency in all directions, although the horizontal fault-perpendicular direction slightly dominates (39%). In the damage zone, the lowest velocity is hardly ever found in the vertical direction (4%), but with almost equal frequency in the two horizontal directions (50 and 46%). In the fluid-alteration zone, the velocity is lowest in the fault-parallel direction in the majority of cases (63%), but rarely in the vertical direction (13%).

4.2.2. Permeability

Permeability was mostly measured in the direction parallel to the strike of the fault, but some measurements were performed in the vertical and in the fault-perpendicular direction (Figure 10a). The permeability of the sample in the southern wall rocks ($x = -100$ m) varies by about 1 order of magnitude depending on the measurement direction, but the permeability of the sample in the southern damage zone at $x = 128$ m is nearly independent of the measurement direction. Samples from the southern and northern damage zones, as well as the southern wall rocks close to the fault zone boundary, exhibit the highest permeabilities on the

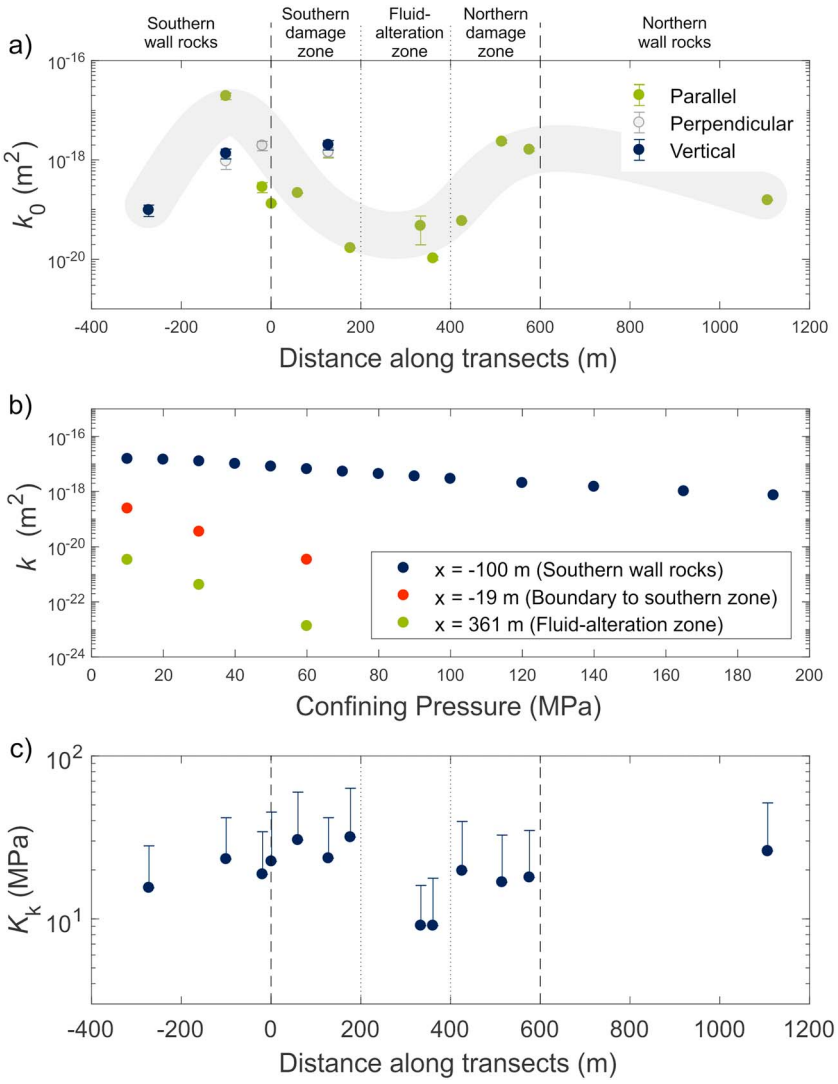

Figure 10. Permeability measurements. (a) Permeability at zero pressure as derived from the measurements of permeability as a function of confining pressure. Color coding refers to the direction of fluid flow in the experiments with respect to the orientation of the fault. Thick light gray line highlights variation of permeability across the fault zone. (b) Dependence of permeability on confining pressure for exemplary samples from the southern wall rocks (blue symbols), from the boundary to the southern damage zone (red symbols), and from the fluid-alteration zone (green symbols). (c) Variation of permeability modulus along transects.

order of 10^{-18} m^2 (Figure 10a). The lowest permeabilities of c. 10^{-20} m^2 were measured on samples from the fluid-alteration zone, while the northern wall rocks (x = 1100 m) have quite high permeability.

The dependence of permeability on confining pressure varies in samples from different parts of the fault zone (Figures 10b and 10c). A sample from the southern wall rocks shows a moderate decrease in permeability with increasing confining pressure (Figure 10b). Permeability moduli from the wall rocks are relatively large with values of 15–26 MPa (Figure 10c). In the southern and northern damage zones, the pressure dependence of permeability is moderate (Figure 10b) and the permeability moduli are highly variable (16–31 MPa; Figure 10c). The data from the wall rocks and the southern and northern damage zones show a decrease in the pressure dependence of permeability with increasing confining pressure (Figure 10b); apparently, all compliant microfractures are closed at a finite pressure such that permeability will not decrease further. This crack-closure pressure is reached at approximately 100 MPa in the wall rocks and 60 MPa in the southern and northern damage zones. In the fluid-alteration zone, the pressure dependence of permeability is highest (Figure 10b) and the permeability modulus is low (c. 9 MPa, Figure 10c).

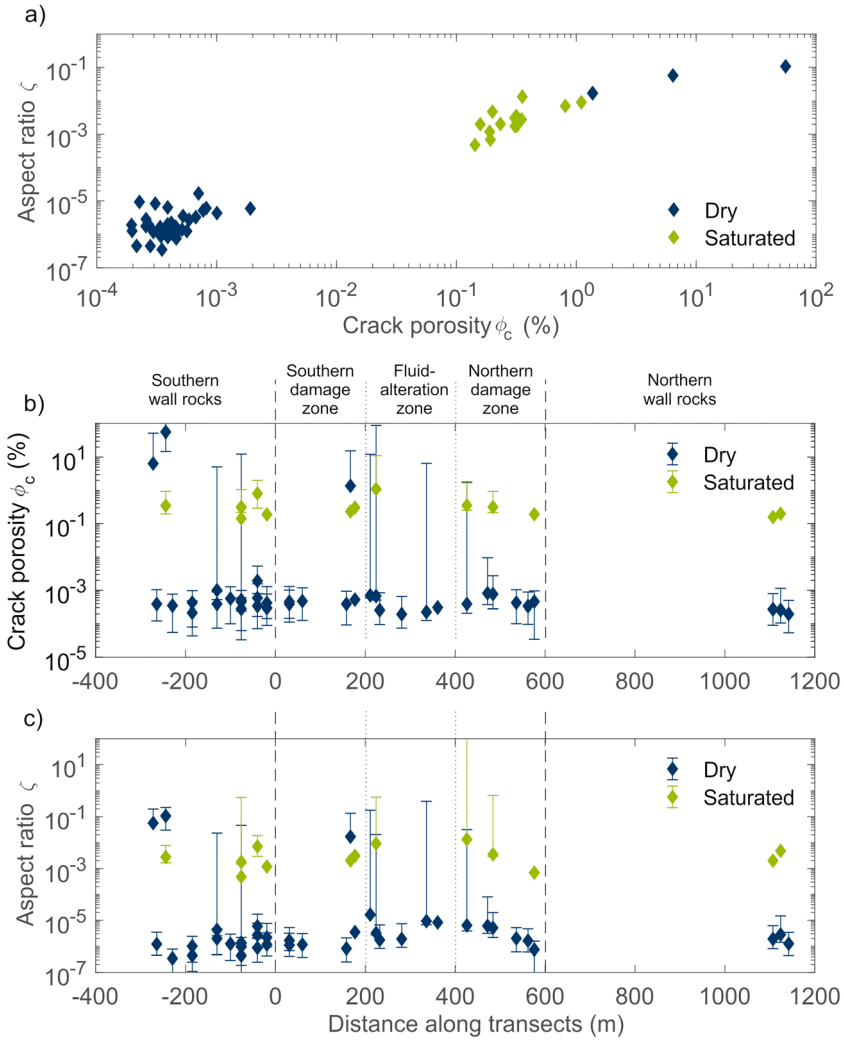

Figure 11. Equivalent crack density and aspect ratio. (a) Modeled equivalent aspect ratio versus equivalent crack porosity for the dry and saturated case derived from modeling normalized *P* and *S* wave velocities, respectively, using equations (7) und (8). (b) Crack porosity and (c) crack aspect ratio versus distance along the transects.

4.3. Modeling Results

4.3.1. Modeled Equivalent Crack Porosity and Aspect Ratio

Equivalent crack porosity and aspect ratio were modeled from the ultrasonic wave velocities on dry and saturated samples (equations (7) and (8)) normalized to the velocities of the background material, $V_{p,0}$ and $V_{s,0}$. The required reference values E_0 and G_0 were determined from the Hill average of the moduli and densities of the constituents of the tonalite (48% plagioclase, 29% quartz, 17% biotite, and 6% K-feldspar; Di Toro & Pennacchioni, 2004) taken from Mavko et al. (1998). The full suite of velocities (*P* and *S* wave velocities on both dry and saturated samples) was only obtained for 27 of the 83 samples, mainly due to difficulties in picking the first arrival of *S* waves.

Modeled equivalent crack porosities differ significantly for dry and saturated samples, yielding values of mainly 10^{-4} to 10^{-3}% for the dry case and 0.1 to 1% for the saturated case (Figures 11a and 11b). Modeled aspect ratios are mainly in the range of 10^{-6} in the dry case and 10^{-3} in the saturated case, with slightly larger values next to and within the fluid-alteration zone (Figures 11a and 11c). For neither dry nor saturated samples do either of the two modeled quantities exhibit a significant correlation with location along the transects (Figures 11b and 11c).

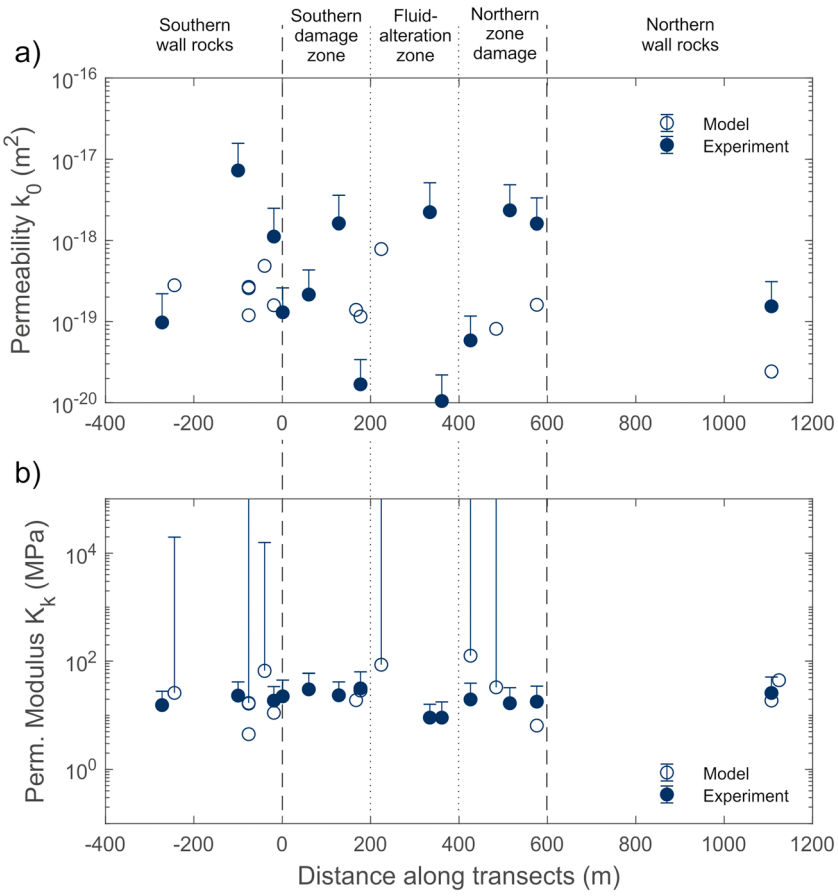

Figure 12. Modeled permeability and permeability modulus (open symbols) compared to experimentally determined values (filled symbols). (a) Permeability and (b) permeability modulus modeled for the saturated case after equations (9) and (11), respectively, versus distance along the transects. A crack aperture of $w = 10^{-2}$ μm was used to model permeability.

4.3.2. Modeled Permeability and Permeability Modulus

The modeled values for effective crack porosity and aspect ratio correspond to interconnectivity parameters $f = 1$, corresponding to full connectivity (equation (10)), for c. 78% of the dry and 43% of the saturated samples. Only 8 and 14% of the dry and saturated samples, respectively, exhibit connectivity parameters $f = 0$. Calculating permeability from equation (9) using the modeled crack parameters still requires choosing a crack aperture. To match the order of magnitude of modeled and experimental permeability (Figure 12a), crack apertures of 100 and 10 nm have to be chosen for the dry and saturated case, respectively. Most of the calculated permeability moduli are between 10^1 and 10^2 MPa and thus in the order of magnitude of the experimentally determined permeability moduli $K_{k,\mathrm{stat}}$ (Figure 10c).

5. Discussion

The constraints on the damage structure of the fault zone gained here by the fracture tracing method and previously by the point-intersection method (Smith et al., 2013) are comparable overall (see Appendix A2 for a detailed discussion of the relation between P_{10} and P_{21}). Microscale damage is relatively symmetric across the fault zone with a generally low degree of damage in the wall rocks and a relatively high degree of damage within the fault zone (Figures 13a and 13b).

In the following sections, we will concentrate on discussing several key questions:

1. How do the elastic and hydraulic properties of the rock samples relate to the intensity of microfractures and their orientation?

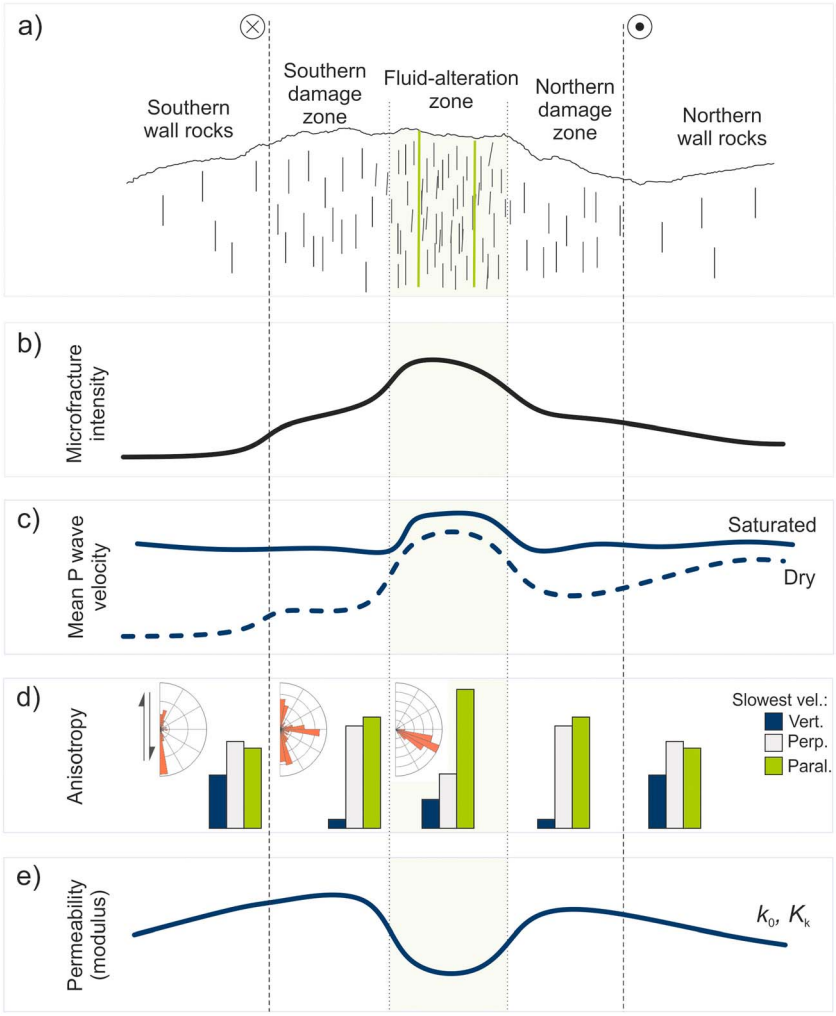

Figure 13. Summary of the damage structure of the GLFZ and the experimentally determined physical properties. (a) Visualization of the fault zone structure. The view has been tilted to the north to account for the dip of the fault zone to the south with a dip angle of c. 60° (see Figure 10 in Smith et al., 2013). Schematic representations of the variation of (b) microfracture intensity (Figure 7) and (c) *P* wave velocity measured on dry and saturated samples (Figure 8). (d) Rose diagrams illustrating the main orientation of microfractures (valid for open microfractures and fluid-inclusion planes) and bar plots showing the percentage of the direction relative to fault strike in which *P* wave velocity was the slowest for the subzones illustrated in (a) (Figure 9). (e) Schematic of the variation of permeability k_0 and permeability modulus K_k across the fault zone (Figure 10).

2. Why do the modeled crack parameters fail to reflect the variation across the fault zone of the experimental values upon which the model is based?
3. What is the influence of alteration and sealing of fractures on the correlation of physical properties and damage and on the applicability of our effective-medium approach to model the microstructural damage?
4. Can we describe the postseismic structure of the fault zone based on the present-day physical and microstructural properties?
5. How do our results contribute to an understanding of the properties of fault zones and their evolution with time?

5.1. Correlation Between Microfracture Damage, Elastic Properties, and Hydraulic Structure of the Gole Larghe Fault Zone

Intensity and orientation of microfractures correlate to some degree with magnitude and anisotropy, respectively, of measured ultrasonic velocities. The ultrasonic *P* wave velocities and to a lesser degree the *S* wave

velocities show an inverse correlation with the microfracture intensity (Figures 13a–13c), irrespective of a preferred orientation of microfractures or a directional dependence of velocities, which is subordinate compared to variation along the transects. Thus, the ultrasonic velocities qualify as a proxy for structure. Velocities are generally high where measured microfracture intensity is low, and vice versa. The fluid-alteration zone, however, constitutes an exception. In this area, the intensity of microfractures is high, but many of the microfractures are sealed leading to relatively high *P* wave velocities. Sealed fractures in the fluid-alteration zone are mainly filled with K-feldspar and epidote (Smith et al., 2013). Epidote has a high intrinsic *P* wave velocity (c. 7,400 m/s; Mavko et al., 2009) and is likely responsible for the increased seismic velocities of rocks from the fluid-alteration zone. Upon saturation of samples with water, the *P* and *S* wave velocity increases to a higher degree for samples from wall rocks and southern and northern damage zone than for those from the fluid-alteration zone (Figures 8a and 13c). The relatively small difference in velocities measured on dry and saturated samples observed for the fluid-alteration zone underlines that sealing affects porosity and microfracture connectivity in this zone.

Microfractures from the wall rocks are mostly oriented parallel to the E-W strike of the fault and are likely formed during the cooling of the tonalite (Figure 13d). Microfractures inside the fault zone that have a range of orientations are most likely due to seismic activity in the Gole Larghe Fault Zone (Griffith et al., 2010). The preferred orientation of FIPs or open microfractures and the anisotropy of the ultrasonic *P* wave velocities appear to correlate to some degree (Figure 13d). In only 15% of all samples, the *P* wave velocity was slowest in the vertical direction (Figures 9a and 13d), which is consistent with mainly steeply dipping microfractures. Microfracture tracings of most samples from the southern wall rocks showed a preferred fault-parallel orientation, which should correspond to lowest velocity perpendicular to the fault. Even though velocity is, in fact, lowest in the fault-perpendicular direction for 39% of the samples from the southern and northern wall rocks (Figure 9b), this velocity anisotropy is not as clear as the preferred orientation shown by the microfracture tracings (Figure 13d). Given the errors of the velocity measurements, the damage anisotropy apparently cannot be resolved by the *P* wave velocities. It cannot be excluded that the velocity anisotropy is influenced by a magmatic foliation present in some parts of the Adamello tonalite (Figure 1; Bianchi et al., 1970), although no foliation was observed in the hand specimens. In addition, if microfractures were subparallel to the fault surface, which has a dip angle of 60°, anisotropy determined for the measurement directions might be decreased with respect to the anisotropy that would be detected if velocities were measured parallel to the dip direction of the fault surface rather than in the vertical direction. Yet for the magnitude of anisotropy measured on our samples, we can exclude deviation of anisotropy exceeding 10% (Appendix A1). Microfracture orientation and velocity anisotropy agree for the damage and fluid-alteration zone. In the southern and northern damage zones, fault-perpendicular fractures—inferred from the velocity measurements—are slightly more common than fault-parallel ones (46 and 50%, respectively), which agrees with the microstructure analysis showing that roughly fault-parallel oriented cooling fractures are joined by approximately fault-perpendicular striking fractures. In the fluid-alteration zone, the percentage of approximately fault-perpendicular fractures inferred from the direction of lowest velocity is significantly higher (63%) than that of roughly fault-parallel (25%) or horizontal (13%) microfractures, consistent with microstructural observations.

The permeability correlates generally well with the degree of microfracture damage and thus the measured velocities (Figure 13e). Permeability is up to 2 orders of magnitude lower for the wall rocks than for the rocks from the northern and southern damage zones. Sealing of microfractures in the fluid-alteration zone leads to permeability approximately 1 order of magnitude lower than for the wall rocks. The pervasive sealing in the fluid-alteration zone suggests that the central part of the fault zone acted as a fluid conduit only transiently. The observed permeability variation across the GLFZ matches with a combined conduit/barrier for fluid flow as defined by Caine et al. (1996). On a smaller scale, the damage zone is a conduit-barrier system in itself, because the damage is distributed relatively heterogeneously inside the damage zone, where slightly damaged rocks are cut by highly damaged cataclastic bands (Smith et al., 2013). Samples were collected from the more intact rocks between major cataclastic faults. The contribution of these cataclastic faults to the bulk permeability of the fault zone is unknown. However, the cataclasites are also pervasively sealed (Di Toro & Pennacchioni, 2004; Smith et al., 2013) and it is likely that their permeability is low and reasonable well approximated by the permeability measurements made on samples from the alteration zone.

The variation of the permeability modulus across the fault zone inversely correlates with the variations in microfracture intensity and ultrasonic *P* and *S* wave velocities (Figures 13b, 13c, and 13e). As velocity and permeability, the permeability modulus, too, is affected by the degree of damage and sealing, because the change in permeability with pressure is governed by the elastic closure of cracks. The variation of the permeability modulus within the wall rocks and southern and northern damage zone is within the error of the modulus. In the fluid-alteration zone, the permeability modulus is significantly lower; that is, the sensitivity of permeability to changes in pressure is high. This reduction in permeability modulus associated with a simultaneous increase in ultrasonic velocity is not readily understandable in the light of the low permeability and high degree of microfracture sealing. However, even a relationship between velocity and permeability depends significantly on the microstructure and is often hard to establish (e.g., Ahrens et al., 2018) and, thus, it is even less straightforward to understand the relationship of velocity and permeability modulus as a second-order variable. The calculation of the permeability modulus (equation (11)) depends solely on the change of the fractures geometry with pressure. An effect of pressure on the crack connectivity is not taken into account. As the low permeability of the samples from the fluid-alteration zone suggests a proximity to the percolation threshold, the high-pressure sensitivity of the permeability might be caused by a pressure dependence of the fracture interconnectivity rather than of the permeability.

5.2. Applicability of the Effective-Medium Model

Equivalent crack porosities and aspect ratios derived from *P* and *S* wave velocities measured on dry and water-saturated samples differ considerably (Figure 11a). The equivalent aspect ratio modeled from ultrasonic velocity measured on saturated samples compares well with aspect ratios derived from microstructural analysis of faulting-induced damage (0.01 to 0.2, Gomila et al., 2016; see also Kranz, 1983), while the aspect ratio for the dry case is several orders of magnitude smaller. Similarly, the crack porosity for the saturated case is $\leq$1% and thus similar to the connected porosity measured in the laboratory (Figure 8). For the dry case, crack porosities are several orders of magnitude smaller than inferred from the laboratory measurements. It has previously been concluded from laboratory experiments that the saturation state has a significant effect on which elements of a distribution of fractures control ultrasonic velocity (Song & Renner, 2008). Even few long fractures seem to be more relevant for velocities of dry than for saturated samples.

The microcrack parameters derived from the ultrasonic velocity measurements do not reflect the systematic variation across the fault zone shown by the ultrasonic velocity (Figures 8 and 11). Kachanov's (1993) approach rests on several assumptions that might be violated. The highly fractured samples from the fluid-alteration zone likely violate the assumption of nonintersecting cracks. The difference in the modeled aspect ratio for dry and saturated samples (Figure 11) indicates that the assumption of *monosized* cracks is too simple as might be that of the penny-shaped crack geometry. Moreover, our microfracture-orientation analysis revealed that cracks are not randomly distributed as assumed by the model (Figures 7a and 13d). However, the isotropic model is consistent with the symmetry classification based on the velocity measurements (c. 70% are isotropic within the measurement error) such that we refrained from using a more involved approach and consider the derived porosity and aspect ratio as semiquantitative parameters apt for comparing all samples.

A further prominent reason for the mismatch of measured properties and modeled equivalent crack porosity is given by the alteration of the rock samples. Heterogeneous alteration poses a problem in the application of the effective-medium approach because it limits the comparability of different samples. If a different degree of alteration is not taken into account in the model by adjusting the background elastic properties, that is, E_0 and G_0, of each sample, the calculated equivalent crack porosity and aspect ratio not only will depend on the density of open microfractures but also will be biased by the variable alteration of the sample material. In this study, uniform background material properties were employed for all samples, that is, one calculated from the bulk mineral composition of the host rock, as adjusting E_0 and G_0 for each sample requires extensive mineralogical characterization. However, our samples show some postdeformational alteration of microfractures. Velocities are therefore influenced not solely by fractures but also by a chemical alteration of the rock material and the sealing of fractures. This issue did not affect the previous laboratory studies, which reported modeling of single samples with well-defined background values because all of these studies investigated the evolution of the rock damage in one sample during laboratory deformation tests (Benson et al., 2006; Blake et al., 2013; Guéguen & Schubnel, 2003; Sayers & Kachanov, 1995; Schubnel et al., 2003, 2006).

Table 3
Parameters V_0, m_{open}, and m_{sealed}, and Correlation Coefficients R^2 Resulting From Multilinear Regression of Measured Ultrasonic Velocities and Intensities of Open and Sealed Microfractures According to Equation (12)

	V_0 (m/s)	m_{open}	m_{sealed}	R^2
$V_{p,dry}$	4,043	−15.1	45.5	0.51
$V_{p,sat}$	5,998	−20.0	12.5	0.29
$V_{s,dry}$	2,376	−7.4	19.4	0.37
$V_{s,sat}$	2,783	4.5	2.9	0.04

The order of magnitude of the permeability modeled according to Dienes (1982) is similar to that of the permeability at zero pressure k_0 determined from the experimental data when using crack apertures of 10–100 nm (Figure 12a). A nanometer-scale crack aperture appears small compared to previous microstructural observations of micrometer-scale apertures (Gomila et al., 2016). It is difficult, however, to identify the elements of a network critical for interconnectivity and thus microstructural observations likely provide an upper bound for aperture at best.

The agreement of the majority of the modeled dynamic permeability moduli $K_{k,dyn}$ with the experimental permeability moduli $K_{k,stat}$ (Figure 12b) is at odds with the expectation that permeability is sensitive to the closure of few critical cracks, while ultrasonic wave velocity is affected by the closure of cracks whether they contribute to interconnectivity or not. Thus, the good agreement between $K_{k,dyn}$ and $K_{k,stat}$ may suggest that the crack networks are characterized by a high interconnectivity in the investigated samples. According to our permeability modeling, a high interconnectivity, that is, f~1 (equation (10)), is given for 45% of saturated and 78% of dry samples.

5.3. Inferred Postseismic Physical Properties

The effect of fracture sealing on the seismic velocity was quantified by a multilinear regression analysis of the measured velocity and the number of open and sealed P_{10} microfractures to infer the *postseismic* structure of the GLFZ. This analysis provides the hypothetical velocity structure of the fault zone for a stage in which all microfractures are open, which may approximate the postseismic state immediately after a large earthquake rupture before mineral precipitation sets in. As a thought experiment, this analysis of the postseismic velocity structure may be relevant to other fault zones damaged during large earthquakes, even though this situation will likely not have occurred for the GLFZ, because the broad fault zone we observe today was likely created by many subsequent ruptures (Di Toro & Pennacchioni, 2004, 2005). In addition, the analysis provides an estimate of the magnitude of the velocity changes caused by fracture sealing.

The hypothetical postseismic velocity structure is predicted assuming linear relationships between the measured velocity V_{eff} and the number of open and sealed microfractures $P_{10,open}$ and $P_{10,sealed}$:

$$V_{eff} = V_0 + m_{open}P_{10,open} + m_{sealed}P_{10,sealed} \quad (12)$$

and determining the values of the coefficients V_0, m_{open}, and m_{sealed} via multilinear regression analysis (Table 3). Using the determined coefficients, the postseismic velocity is calculated by assuming that all fractures are open, that is, $P_{10,open} = P_{10,total}$ and $P_{10,sealed} = 0$. The resulting effective velocity structure is quite symmetric, with a pronounced decrease in P wave velocity toward the center of the fault zone (Figure 14a). The different zones of the fault area, that is, wall rocks, southern and northern damage zone and central zone (which is not yet a *fluid-alteration* zone) can still be distinguished from the variation in velocity. The structure depicted by $V_{p,sat}$ and $V_{s,dry}$is similar to that of $V_{p,dry}$, while $V_{s,sat}$ increases toward the centre of the fault zone (Figures 14b–14d).

The postseismic velocities measured on saturated samples—relevant for natural conditions—are used to model the equivalent postseismic crack porosity and aspect ratio (Figure 15). The equivalent crack porosity reflects the systematic variation of the total microfracture intensity across the fault zone: crack porosities are generally low in the wall rocks, intermediate in the southern and northern damage zones, and highest in the fluid-alteration zone (Figure 15a). Modeled aspect ratios are in the range of 10^{-3} to 10^{-2}, correlating well with values reported in the literature (Gomila et al., 2016; Kranz, 1983; Figure 15b). Two outliers that fall into the fluid-alteration zone are caused by two exceptionally low S wave velocity values measured on samples from this distance along the transects (Figure 8).

The correlation coefficients R^2 of the multilinear-regression analysis are rather low for $V_{p,dry}$, $V_{p,sat}$, and $V_{s,dry}$, but particularly so for $V_{s,sat}$ (Table 3). Poor correlation might, in general, reflect that the linear model is too simple to describe the relationship between microfracture intensity and velocity. The extremely low correlation coefficient for $V_{s,sat}$ specifically reflects the sparsity of data points for this case, and the counterintuitive

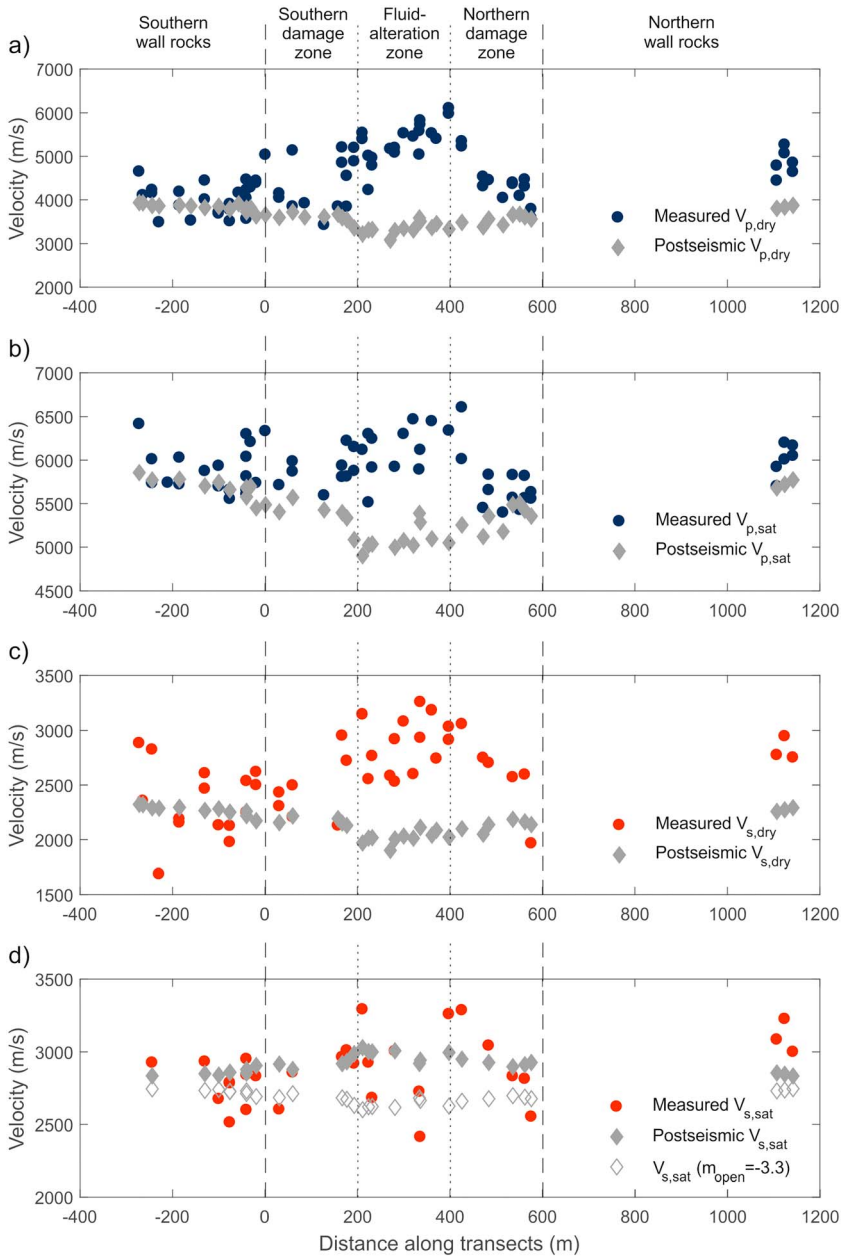

Figure 14. Inferred *postseismic P* and *S* wave velocity assuming that no microfractures are sealed (gray diamonds) compared to velocities measured on saturated samples (blue and red circles). Postseismic velocities were calculated via multilinear regression of velocity and numbers of open and sealed microfractures (equation (12) and Table 3).

positive correlation between *S* wave velocity of saturated samples with fracture intensity of open cracks (Table 3 and Figure 14d) is thus not significant. When considering a more intuitive case in which $V_{s,sat}$ decreases with increasing open microfracture intensity (i.e., when selecting a negative coefficient $m_{open} = -3.3$ within the standard error gained from the regression analysis; Figure 14d), the modeled equivalent crack porosity still reflects the variation of the damage across the fault zone (Figure 15).

The correlation of equivalent postseismic crack porosities and measured total microfracture intensities indicates that our model might, in fact, work well with unaltered samples such as experimentally deformed rocks. When inverting velocities from field studies to derive information on structure, however, results might be affected significantly by alteration. Thus, a heterogeneous background model of elastic properties should

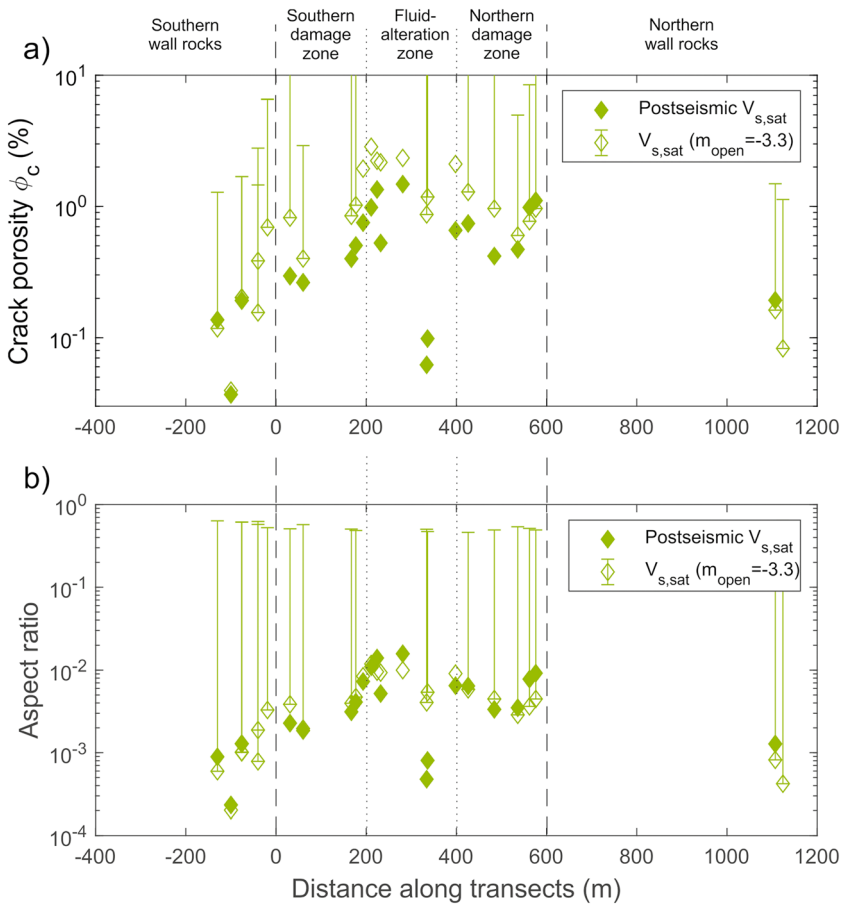

Figure 15. Crack parameters modeled from the postseismic velocities. (a) Crack porosity and (b) aspect ratio versus distance along the transects. Filled symbols represent data modeled directly from postseismic velocities, that is, using the positive coefficient $m_{open} = 4.5$, open symbols those modeled using a negative coefficient $m_{open} = -3.3$ (open symbols in Figures 14d).

be used which, for example, might be based on estimates of the degree of alteration and sealing of the rock from geological studies of the field area.

As ultrasound velocity measurements, our permeability measurements provide only a snapshot of the damage state of the GLFZ, too. Fluid flow yields a progressive alteration and sealing of microfractures and causes an evolution of the damage state of faults over time. Thus, the postseismic permeability of the rocks from damage and fluid-alteration zone was likely higher than it is today after healing and sealing of fractures, that is, larger than $2 \cdot 10^{-17}$ m^2, the highest permeability measured on a sample from the damage zone (Figure 10a). When estimating the permeability at depth, the effect of the elastic closure of cracks has to be taken into account. Considering an average of the experimentally determined permeability modulus of 23 MPa^{-1} for the damage zone rocks and assuming that the permeability does not decrease significantly at pressures higher than the crack-closure pressure (c. 60–100 MPa; Figure 10b), the permeability at depth following rupture is estimated to be higher than $3 \cdot 10^{-19}$ m^2. The sealing characteristics we observe today imply that this magnitude of permeability will have allowed for local fluid flow at depth.

5.4. Implications for Geophysical Studies of Fault Zones

We observed a dependence of elastic wave velocity on microfracture damage and the degree of microfracture sealing within the Gole Larghe Fault Zone. Based on this relation, we modeled a possible evolution of the wave velocity with time due to crack sealing and healing. Several studies have reported a recovery of seismic wave velocities in fault zones or a change in the characteristics of seismic signals over a timescale of 2–5 years following a velocity-reducing earthquake (Baisch & Bokelmann, 2001; Hiramatsu, 2005; Li et al., 1998; Li &

Vidale, 2001; Schaff & Beroza, 2004; Tadokoro & Ando, 2002), although there is also evidence that fracture damage can persist for hundreds of years following some earthquake ruptures (Cochran et al., 2009). Possible causes for a relatively rapid recovery (2–5 years) of seismic velocity include crack healing, diffusion of fluids into the fault zone, and fault-normal compaction, all of which would yield a *stiffer* fault zone. In situ velocities were generally found to recover as a function of the logarithm of time, implying that recovery of fault strength was rapid directly following the earthquake, although full recovery could not be observed in the relatively-short term studies (Li & Vidale, 2001; Schaff & Beroza, 2004). Li and Vidale (2001) show that a decrease in crack density of a few percent could explain the observed increase in wave velocity (also of a few percent), while other authors suggest that cracks can be fully healed within a period of 2 years following rupture (Hiramatsu, 2005). Actual crack *healing* occurs by diffusional processes on the crystal scale leaving (secondary) fluid-inclusion planes as evidence of the initial crack surface (Smith & Evans, 1984; Sprunt & Nur, 1979). At depth, this process can occur on a timescale of days (Smith & Evans, 1984; see also Klevakina et al., 2014) and might explain the recovery of the in situ seismic wave velocities. Additionally, closure of cracks due to confining pressure or loss of fluid (pressure) diminishes the influence of the cracks on the elastic properties of the material without a healing process.

Microstructure analysis of our samples showed that both healing and sealing of microfractures occurred in the Gole Larghe Fault Zone. As a consequence of fracture sealing by secondary minerals with a high intrinsic seismic wave velocity (i.e., epidote), ultrasonic velocity was significantly increased. This significant velocity increase in highly fractured samples is observed even though only a fraction of cracks is sealed and a large proportion of fractures remains open. Therefore, sealing of fractures might explain the seismologically observed strength recovery and might eventually even yield an exceedance of the pre-event velocity values. However, the ultrasonic measurements probed the damage only on the microscale. A scale dependence of the velocity is generally found when field and laboratory measurements were compared in cases where damage was present (Jeanne et al., 2012; Rempe et al., 2013; Vinciguerra et al., 2006). The scale dependence of velocity is caused by the different frequencies of the ultrasonic waves used in laboratory tests and those generated in seismic surveys, as they are affected differently by microscale and macroscale damage. When collecting samples in the field, we avoided large-scale cataclasite- and pseudotachylyte-bearing fault strands. These fault strands represent a small percentage of the total volume of the fault rocks and would likely not be *seen* by the meter-scale wavelength employed by seismic studies. Thus, our sampling technique will have reduced the effect of velocity scale dependence to some degree. It is therefore likely that (i) ultrasonic velocity variation derived from the samples and (ii) the modeling results using Kachanov's theory (which is independent of frequency) represent the variation of elastic fault zone properties and microstructural parameters, respectively, as they would be probed by in situ studies. However, some scale dependence will prevail because it is unlikely that the sealing of (sub)millimeter-scale microfractures would affect field-scale data to the same degree as the laboratory-scale data.

In summary, the correlation between microfracture intensity and physical properties found for the Gole Larghe Fault Zone shows that ultrasonic measurements of the seismic velocity potentially serve as a proxy for microfracture damage and permit at least a qualitative estimation of the variation of permeability with the degree of damage. The correlation between microfracture orientation and velocity anisotropy may provide the basis to use velocity measurements as paleostress indicators and as the orientation of microfractures of seismic origin reflects the stress state at the tip of the propagating (earthquake) rupture, to evaluate earthquake rupture models (Faulkner et al., 2010; Mitchell & Faulkner, 2009; Scholz et al., 1993; Vermilye & Scholz, 1998). Alteration poses a problem to the interpretation of the seismic velocities and limits the applicability of models used to infer the damage structure. More work is needed to differentiate the—possibly competing—effects on the velocity of postseismic stress and fluid pressure changes, fracture sealing, alteration, and mechanical crack closure due to aging. In addition, some microstructural analysis should always be carried out to gain a comprehensive view of the fault's damage structure and to allow for the interpretation of in situ seismic data.

6. Conclusions

The damage structure of the Gole Larghe Fault Zone, a 600-m-wide exhumed seismogenic strike-slip fault in the Italian Southern Alps, was characterized by investigating the microstructure, ultrasonic wave velocity, and permeability of samples collected along a 1.5-km-long transect. Porosity, velocity, and permeability show

systematic variations across the fault zone that correlate well with the observed microfracture intensity. A low degree of damage is generally associated with low permeability and high ultrasonic velocities and vice versa. Variations in velocity across the fault zone are consistent with previously established subzones based on the degree of damage, that is, southern and northern damage zones and a central fluid-alteration zone. The latter exhibits pervasive alteration and fracture sealing by epidote and K-feldspar. The anisotropy of microscale damage and of the velocities measured in three orthogonal directions correlate to some degree, indicating that fractures are subvertical and more often oriented fault-perpendicular than fault-parallel in the fluid-alteration zone.

Micromechanically modeled equivalent crack porosity, crack aspect ratio and permeability lie in a physical possible range, but they do not show the expected variation across the fault zone that is shown by the laboratory measurements of seismic velocities on which the model is based. As velocities are not solely influenced by fractures but also by an alteration of the background material and its elastic properties, the alteration of the rocks and sealing of fractures provides a limitation in the applicability of the model to natural rocks that also has to be considered when interpreting in situ seismic measurements or seismological observations such as fault healing following earthquakes. Quantifying the effect of alteration on the seismic velocities provides the opportunity to model the equivalent crack porosity. It is thus inevitable to perform some—at least qualitative—mineralogical characterization to distinguish intact rocks from damaged rocks which experienced extensive sealing.

Appendix A

A1. Orientation Bias and Uncertainty of Microfracture Intensities

As measured fracture intensity is a function of the angle of intersection between the fracture and the plane of observation, the intensity of the microfractures obtained from their intersections either with a 1-D horizontal scan line or the horizontal plane needs to be corrected (Terzaghi, 1965). Considering the angle between the dip of the Gole Larghe Fault Zone and the vertical is 30° and assuming that the majority of microfractures are subparallel to the fault plane, thus exhibiting the same dip, the corrected fracture intensity is determined by $P_{10,corr} = P_{10}/\sin(60°) \simeq 1.2P_{10}$ (following Terzaghi, 1965); that is, the fracture intensity corrected in this way does not deviate significantly from the original counts (Figure A1). However, as the true dip of the microfractures is not known and, in fact, will likely not be a constant but be more accurately described by a distribution function, we refrain from a correction of the fracture intensities and instead estimate the uncertainty. The uncertainty of P_{10} microfracture intensity was quantified following the procedure of Lu et al. (2017), which considers errors in the determination of the intensity due the relative orientation of fractures and scan line (*sampling error*) and statistical fluctuation of the intensity from one sample to another caused by the scan line length (*estimation error*; Einstein & Baecher, 1983). The uncertainty can be calculated from the length L of the test line and the number of fracture intersections $E(P_{10})$ with the test line assuming that the uncertainty of fracture intensities can be expressed through the variance of a Poisson distribution (Lu et al., 2017). The standard deviation of the fracture intensities is then given by

$$\sigma(P_{10}) = L^{-0.5}E(P_{10})^{0.5}, \tag{A1}$$

from which the upper and lower bounds of the 90% confidence interval for the fracture intensities can be calculated. These upper and lower bounds for $L = 0.8$ mm are plotted as error bars to the total microfracture intensity in Figure 7a. These error bars provide a conservative estimation of the uncertainty as here we associate the length of a single test line with the total number of fractures derived from all the test lines in one sample. The error resulting from our calculation will therefore be larger than when calculated from the number of fractures associated with a specific test line of a certain length, which unfortunately we did not record, nor did we record the number of test lines per sample. However, as further uncertainty is introduced due to the likely misreading of some fractures (*measurement error*, Einstein & Baecher, 1983) and the invisibility of small fractures (*truncation bias*), we suggest that the conservative uncertainty may nevertheless be accurate. The uncertainty of P_{21} microfracture intensity (Figure 7a) was estimated assuming a 10% error due to the orientation bias, the estimation error, measurement errors due to misreading of some microstructures, and the truncation bias associated with small fractures.

The effect of the measurement direction on the deduced degree of anisotropy was estimated by assuming a transversely isotropic case where the axis of symmetry is oriented parallel to fault surface; that is, it dips with

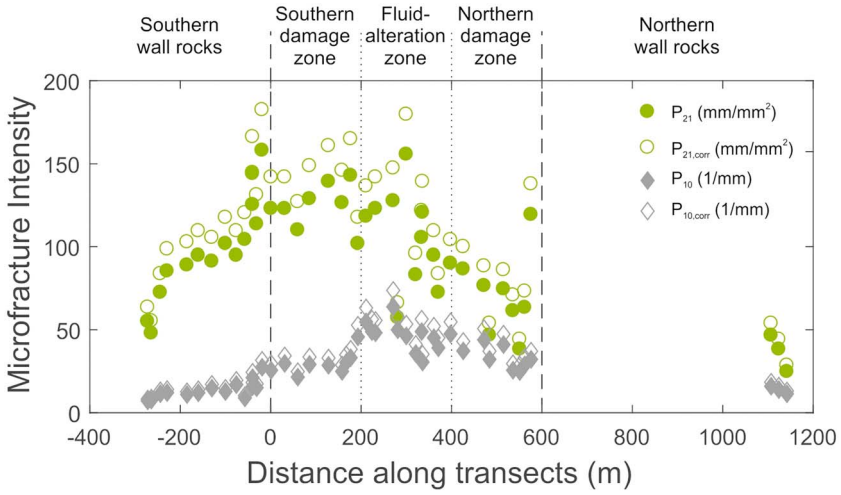

Figure A1. Terzaghi-corrected microfracture intensity. Comparison of original P_{21} and P_{10} fracture intensities (full symbols) and that corrected for an orientation bias (open symbols) using a correction factor of 1.155 following Terzaghi (1965).

60°. The ratio of the velocity measured parallel to the axis of symmetry, $v_p(\theta = 0°)$, and in the plane of symmetry, $v_p(\theta = 90°)$, yields the true degree of anisotropy. The velocity measurements in the truly vertical direction and in the two orthogonal horizontal directions as conducted for this study are shifted by $\theta = 30°$ from the axes of the transversely isotropic medium. The apparent degree of anisotropy for P wave velocity $A_{P,app}$ is thus given by

$$A_{P,app} = \frac{v_p(\theta = 30°)}{v_p(\theta = 60°)} = \sqrt{\frac{A\sin^2(30°) + C\cos^2(30°) + L + \sqrt{M(30°)}}{A\sin^2(60°) + C\cos^2(60°) + L + \sqrt{M(60°)}}} \quad \text{(A2)}$$

where $M = [(A - L)\sin^2\theta - (C - L)\cos^2\theta]^2 + (F + L)^2\sin^2 2\theta$, and A, C, L, and F represent the elastic constants for transverse isotropy (Mavko et al., 1998).

A2. Comparison of P_{10} and P_{21} Microfracture Intensities

Microfracture intensity analysis using the point-intersection (P_{10}) method performed by Smith et al. (2013) was complemented in this study by the length-per-area (P_{21}) method. According to stereological considerations, the relation between the length of randomly oriented lineal elements in a plane and their intersection with a test line is given by $P_{21} = P_{10}\pi/2$ (Mauldon & Dershowitz, 2000; Nemati & Stroeven, 2001). However, the P_{21} values obtained from our samples exceed the P_{10} values by more than $\pi/2$ and a linear relation between them is not observed (Figure 7a). This might be due to several reasons:

1. P_{10} values were only obtained for quartz grains, while P_{21} values were determined on the whole area of the thin section possibly affecting the fracture orientation and biasing the microfracture intensity.
2. The microfracture orientations obtained from the traced thin-section images show that the assumption of randomly oriented microfractures is clearly not justified (Figure 7a). When using the P_{10} method, the test line was randomly oriented and several counts (in c. 40 quartz grains/sample) were performed for one samples, which diminishes the effect of a preferred microfracture orientation on the obtained intensity, but preferred microfracture orientations might still be responsible for some of the observed discrepancy between P_{10} and P_{21} values.
3. P_{21} values were obtained from microphotographs with a higher resolution than was used for the determination of the P_{10} microfracture intensity. Thus, very thin or short fractures are likely only included in the P_{21} values.
4. As the two measures of microfracture intensity were not obtained on the exact same areas of the thin sections, heterogeneity of the rock may play a role in the difference between absolute P_{10} and P_{21} values and their relative trends.

Results from both methods show that microscale damage is relatively symmetric across the fault zone with a generally low degree of damage in the wall rocks and a relatively high degree of damage within the fault zone. In the center of the fault zone, the fluid-alteration zone is characterized by a higher percentage of sealed microfractures obtained by the P_{10} method (notably containing both sealed fractures and FIPs; Figure 7a). However, this higher percentage is not clearly observed in the P_{21} values for sealed fractures or FIPs (Figures 7a and 7b). The variation in open microscale damage determined with the P_{10} method (Figure 7a) is mirrored in that of the connected porosity (Figure 8a), although there is some scatter in the porosity of samples from the fluid-alteration zone, which supports the idea of sample heterogeneity being responsible for the difference in P_{10} and P_{21} values in this zone. Despite the differences in microfracture intensities measured using the P_{10} and P_{21} methods, overall, the results regarding the damage structure of the fault zone are comparable.

Acknowledgments
Frank Bettenstedt is thanked for technical assistance in the Experimental Geophysics Laboratory of Ruhr-Universität Bochum. We thank two anonymous reviewers and the editors for their valuable comments. T. M. and J. R. are grateful for funding by the German Science Foundation (SFB526). T.M. acknowledges support from NERC grant ref NE/M004716/1. G.D.T. acknowledges funding by the ERC Consolidator grant 614705 NOFEAR. All data used in the manuscript are presented in the figures and tables.

References

Ahrens, B., Duda, M., & Renner, J. (2018). Relations between hydraulic properties and ultrasonic velocities during brittle failure of a low-porosity sandstone in laboratory experiments. *Geophysical Journal International*, *212*(1), 627–645. https://doi.org/10.1093/gji/ggx419

Anders, M. H., Laubach, S. E., & Scholz, C. H. (2014). Microfractures: A review. *Journal of Structural Geology*, *69*, 377–394. https://doi.org/10.1016/j.jsg.2014.05.011

Baisch, S., & Bokelmann, G. H. (2001). Seismic waveform attributes before and after the Loma Prieta earthquake: Scattering change near the earthquake and temporal recovery. *Journal of Geophysical Research*, *106*(B8), 16,323–16,337. https://doi.org/10.1029/2001JB000151

Bennion, D., & Goss, M. (1971). A sinusoidal pressure response method for determining the properties of a porous medium and its in-situ fluid, paper presented at Fall Meeting of the Society of Petroleum Engineers of AIME, Society of Petroleum Engineers.

Benson, P., Schubnel, A., Vinciguerra, S., Trovato, C., Meredith, P., & Young, R. P. (2006). Modeling the permeability evolution of microcracked rocks from elastic wave velocity inversion at elevated isostatic pressure. *Journal of Geophysical Research*, *111*, B04202. https://doi.org/10.1029/2005JB003710

Bernabé, Y., Mok, U., & Evans, B. (2006). A note on the oscillating flow method for measuring rock permeability. *International Journal of Rock Mechanics and Mining Sciences*, *43*(2), 311–316. https://doi.org/10.1016/j.ijrmms.2005.04.013

Berryman, J. G., & Milton, G. W. (1988). Microgeometry of random composites and porous media. *Journal of Physics D: Applied Physics*, *21*(1), 87–94. https://doi.org/10.1088/0022-3727/21/1/013

Bianchi, A., Callegari, E., & Jobstraibizer, P. (1970). *I tipi petrografici fondamentali del plutone dell'Adamello: Tonaliti, quarzodioriti, granodioriti e loro varietà leucocrate*. Padova: Consiglio Nazionale delle Ricerche, Centrodi Studio per la Geologia e la Petrologia delle Formazioni Cristalline.

Blake, O., Faulkner, D., & Rietbrock, A. (2013). The effect of varying damage history in crystalline rocks on the P-and S-wave velocity under hydrostatic confining pressure. *Pure and Applied Geophysics*, *170*(4), 493–505. https://doi.org/10.1007/s00024-012-0550-0

Bradbury, K., Barton, D., Solum, J., Draper, S., & Evans, J. P. (2007). Mineralogic and textural analyses of drill cuttings from the San Andreas Fault Observatory at Depth (SAFOD) boreholes: Initial interpretations of fault zone composition and constraints on geologic models. *Geosphere*, *3*(5), 299–318. https://doi.org/10.1130/GES00076.1

Budiansky, B., & O'Connell, R. J. (1976). Elastic moduli of a cracked solid. *International Journal of Solids and Structures*, *12*(2), 81–97. https://doi.org/10.1016/0020-7683(76)90044-5

Byerlee, J. (1990). Friction, overpressure and fault normal compression. *Geophysical Research Letters*, *17*(12), 2109–2112. https://doi.org/10.1029/GL017i012p02109

Caine, J. S., Evans, J. P., & Forster, C. B. (1996). Fault zone architecture and permeability structure. *Geology*, *24*(11), 1025. https://doi.org/10.1130/0091-7613(1996)024<1025:FZAAPS>2.3.CO;2

Chester, F. M., Evans, J. P., & Biegel, R. L. (1993). Internal structure and weakening mechanisms of the San Andreas Fault. *Journal of Geophysical Research*, *98*(B1), 771–786. https://doi.org/10.1029/92JB01866

Childs, C., Manzocchi, T., Walsh, J. J., Bonson, C. G., Nicol, A., & Schöpfer, M. P. (2009). A geometric model of fault zone and fault rock thickness variations. *Journal of Structural Geology*, *31*(2), 117–127. https://doi.org/10.1016/j.jsg.2008.08.009

Cochran, E. S., Li, Y. G., Shearer, P. M., Barbot, S., Fialko, Y., & Vidale, J. E. (2009). Seismic and geodetic evidence for extensive, long-lived fault damage zones. *Geology*, *37*(4), 315–318. https://doi.org/10.1130/g25306a.1

Dal Piaz, G. V., Bistacchi, A., & Massironi, M. (2003). Geological outline of the Alps. *Episodes*, *26*(3), 175–180.

David, C., Wong, T.-F., Zhu, W., & Zhang, J. (1994). Laboratory measurement of compaction-induced permeability change in porous rocks: Implications for the generation and maintenance of pore pressure excess in the crust. *Pure and Applied Geophysics*, *143*(1–3), 425–456. https://doi.org/10.1007/BF00874337

Del Moro, A., Pardini, G., Quercioli, C., Villa, I., & Callegari, E. (1983). Rb/Sr and K/Ar chronology of Adamello granitoids, southern Alps. *Memorie della Societa Geologica Italiana*, *26*(285), e299.

Di Toro, G., Nielsen, S., & Pennacchioni, G. (2005). Earthquake rupture dynamics frozen in exhumed ancient faults. *Nature*, *436*(7053), 1009–1012. https://doi.org/10.1038/nature03910

Di Toro, G., & Pennacchioni, G. (2004). Superheated friction-induced melts in zoned pseudotachylytes within the Adamello tonalites (Italian Southern Alps). *Journal of Structural Geology*, *26*(10), 1783–1801. https://doi.org/10.1016/j.jsg.2004.03.001

Di Toro, G., & Pennacchioni, G. (2005). Fault plane processes and mesoscopic structure of a strong-type seismogenic fault in tonalites (Adamello batholith, Southern Alps). *Tectonophysics*, *402*(1–4), 55–80. https://doi.org/10.1016/j.tecto.2004.12.036

Di Toro, G., Pennacchioni, G., & Nielsen, S. (2009). Pseudotachylytes and earthquake source mechanics. *International Geophysics*, *94*, 87–133. https://doi.org/10.1016/S0074-6142(08)00005-3

Dienes, J. K. (1982). Permeability, percolation and statistical crack mechanics, paper presented at The 23rd US Symposium on Rock Mechanics (USRMS), American Rock Mechanics Association.

Einstein, H. H., & Baecher, G. B. (1983). Probabilistic and statistical methods in engineering geology. *Rock Mechanics and Rock Engineering*, *16*(1), 39–72. https://doi.org/10.1007/BF01030217

Faulkner, D. R., Jackson, C. A. L., Lunn, R. J., Schlische, R. W., Shipton, Z. K., Wibberley, C. A. J., & Withjack, M. O. (2010). A review of recent developments concerning the structure, mechanics and fluid flow properties of fault zones. *Journal of Structural Geology*, *32*(11), 1557–1575. https://doi.org/10.1016/j.jsg.2010.06.009

Faulkner, D. R., Lewis, A. C., & Rutter, E. H. (2003). On the internal structure and mechanics of large strike-slip fault zones: Field observations of the Carboneras fault in southeastern Spain. *Tectonophysics*, *367*(3–4), 235–251. https://doi.org/10.1016/s0040-1951(03)00134-3

Fischer, G. (1992). The determination of permeability and storage capacity: Pore pressure oscillation method. *International Geophysics Series*, *51*, 187–187. https://doi.org/10.1016/S0074-6142(08)62823-5

Gavrilenko, P., & Guéguen, Y. (1989). Pressure dependence of permeability: A model for cracked rocks. *Geophysical Journal International*, *98*(1), 159–172. https://doi.org/10.1111/j.1365-246X.1989.tb05521.x

Gomila, R., Arancibia, G., Mitchell, T. M., Cembrano, J. M., & Faulkner, D. R. (2016). Palaeopermeability structure within fault-damage zones: A snap-shot from microfracture analyses in a strike-slip system. *Journal of Structural Geology*, *83*, 103–120. https://doi.org/10.1016/j.jsg.2015.12.002

Griffith, W. A., Nielsen, S., Di Toro, G., & Smith, S. A. F. (2010). Rough faults, distributed weakening, and off-fault deformation. *Journal of Geophysical Research*, *115*, B08404. https://doi.org/10.1029/2009JB006925

Guéguen, Y., & Dienes, J. (1989). Transport properties of rocks from statistics and percolation. *Mathematical Geology*, *21*(1), 1–13. https://doi.org/10.1007/BF00897237

Guéguen, Y., & Schubnel, A. (2003). Elastic wave velocities and permeability of cracked rocks. *Tectonophysics*, *370*(1–4), 163–176. https://doi.org/10.1016/s0040-1951(03)00184-7

Hiramatsu, Y. (2005). Seismological evidence on characteristic time of crack healing in the shallow crust. *Geophysical Research Letters*, *32*, L09304. https://doi.org/10.1029/2005GL022657

Houston, H. (1990). Broadband source spectrum, seismic energy, and stress drop of the 1989 Macquarie Ridge earthquake. *Geophysical Research Letters*, *17*(7), 1021–1024. https://doi.org/10.1029/GL017i007p01021

Jeanne, P., Guglielmi, Y., & Cappa, F. (2012). Multiscale seismic signature of a small fault zone in a carbonate reservoir: Relationships between VP imaging, fault zone architecture and cohesion. *Tectonophysics*, *554-557*, 185–201. https://doi.org/10.1016/j.tecto.2012.05.012

Jeppson, T. N., Bradbury, K. K., & Evans, J. P. (2010). Geophysical properties within the San Andreas Fault Zone at the San Andreas Fault Observatory at Depth and their relationships to rock properties and fault zone structure. *Journal of Geophysical Research*, *115*, B12423. https://doi.org/10.1029/2010JB007563

Kachanov, M. (1993). Elastic solids with many cracks and related problems. *Advances in Applied Mechanics*, *30*, 259–445. https://doi.org/10.1016/S0065-2156(08)70176-5

Kanamori, H., & Allen, C. R. (1986). Earthquake repeat time and average stress drop. *Earthquake source mechanics*, *37*, 227–235.

Klevakina, K., Renner, J., Doltsinis, N., & Adeagbo, W. (2014). Transport processes at quartz-water interfaces: Constraints from hydrothermal grooving experiments. *Solid Earth Discussions*, *5*(2), 883–899. https://doi.org/10.5194/se-5-883-2014

Knipe, R. (1992). Faulting processes and fault seal. In *Structural and tectonic modelling and its application to petroleum geology* (pp. 325–342). Amsterdam: Elsevier.

Kranz, R., Saltzman, J., & Blacic, J. (1990). Hydraulic diffusivity measurements on laboratory rock samples using an oscillating pore pressure method, paper presented at International Journal of Rock Mechanics and Mining Sciences & Geomechanics Abstracts, Elsevier.

Kranz, R. L. (1983). Microcracks in rocks: A review. *Tectonophysics*, *100*(1–3), 449–480. https://doi.org/10.1016/0040-1951(83)90198-1

Kuster, G. T., & Toksöz, M. N. (1974). Velocity and attenuation of seismic waves in two-phase media: Part I. Theoretical formulations. *Geophysics*, *39*(5), 587–606. https://doi.org/10.1190/1.1440450

Lee, J.-C., Chen, Y.-G., Sieh, K., Mueller, K., Chen, W.-S., Chu, H.-T., et al. (2001). A vertical exposure of the 1999 surface rupture of the Chelungpu fault at Wufeng, western Taiwan: Structural and paleoseismic implications for an active thrust fault. *Bulletin of the Seismological Society of America*, *91*(5), 914–929.

Li, Y.-G., Leary, P., Aki, K., & Malin, P. (1990). Seismic trapped modes in the Oroville and San Andreas fault zones. *Science*, *249*(4970), 763–766. https://doi.org/10.1126/science.249.4970.763

Li, Y. G., & Malin, P. E. (2008). San Andreas Fault damage at SAFOD viewed with fault-guided waves. *Geophysical Research Letters*, *35*, L08304. https://doi.org/10.1029/2007GL032924

Li, Y. G., & Vidale, J. E. (2001). Healing of the shallow fault zone from 1994–1998 after the 1992 *M*7. 5 Landers, California, earthquake. *Geophysical Research Letters*, *28*(15), 2999–3002. https://doi.org/10.1029/2001GL012922

Li, Y.-G., Vidale, J. E., Aki, K., Xu, F., & Burdette, T. (1998). Evidence of shallow fault zone strengthening after the 1992 *M*7. 5 Landers, California, earthquake. *Science*, *279*(5348), 217–219. https://doi.org/10.1126/science.279.5348.217

Li, Y. G., Vidale, J. E., & Cochran, E. S. (2004). Low-velocity damaged structure of the San Andreas Fault at Parkfield from fault zone trapped waves. *Geophysical Research Letters*, *31*, L12S06. https://doi.org/10.1029/2003GL019044

Lu, Y., Tien, Y., & Juang, C. (2017). Uncertainty of 1-D fracture intensity measurements. *Journal of Geophysical Research: Solid Earth*, *122*, 9344–9358. https://doi.org/10.1002/2016JB013620

Mauldon, M., & Dershowitz, W. (2000). A multi-dimensional system of fracture abundance measures, paper presented at Geological Society of America Abstracts with Programs.

Mavko, G., Mukerji, T., & Dvorkin, J. (1998). *Rock physics handbook: Tools for seismic interpretation in porous media*. Cambridge, UK: Cambridge University Press.

Mavko, G., Mukerji, T., & Dvorkin, J. (2009). *The rock physics handbook: Tools for seismic analysis in porous media* (p. 329). Cambridge, UK: Cambridge Univ. Press.

Mitchell, T. M., & Faulkner, D. R. (2008). Experimental measurements of permeability evolution during triaxial compression of initially intact crystalline rocks and implications for fluid flow in fault zones. *Journal of Geophysical Research*, *113*, B11412. https://doi.org/10.1029/2008JB005588

Mitchell, T. M., & Faulkner, D. R. (2009). The nature and origin of off-fault damage surrounding strike-slip fault zones with a wide range of displacements: A field study from the Atacama fault system, northern Chile. *Journal of Structural Geology*, *31*(8), 802–816. https://doi.org/10.1016/j.jsg.2009.05.002

Mitchell, T. M., & Faulkner, D. R. (2012). Towards quantifying the matrix permeability of fault damage zones in low porosity rocks. *Earth and Planetary Science Letters*, *339-340*, 24–31. https://doi.org/10.1016/j.epsl.2012.05.014

Mittempergher, S., Dallai, L., Pennacchioni, G., Renard, F., & Di Toro, G. (2014). Origin of hydrous fluids at seismogenic depth: Constraints from natural and experimental fault rocks. *Earth and Planetary Science Letters*, *385*, 97–109. https://doi.org/10.1016/j.epsl.2013.10.027

Mittempergher, S., Pennacchioni, G., & Di Toro, G. (2009). The effects of fault orientation and fluid infiltration on fault rock assemblages at seismogenic depths. *Journal of Structural Geology*, *31*(12), 1511–1524. https://doi.org/10.1016/j.jsg.2009.09.003

Mooney, W. D., & Ginzburg, A. (1986). Seismic measurements of the internal properties of fault zones. *Pure and Applied Geophysics*, *124*(1-2), 141–157. https://doi.org/10.1007/BF00875723

Morrow, C., Moore, D. E., & Lockner, D. (2001). Permeability reduction in granite under hydrothermal conditions. *Journal of Geophysical Research*, *106*(B12), 30,551–30,560. https://doi.org/10.1029/2000JB000010

Nemati, K. M., & Stroeven, P. (2001). Stereological analysis of micromechanical behavior of concrete. *Materials and Structures*, *34*(8), 486–494. https://doi.org/10.1007/BF02486497

O'Connell, R. J., & Budiansky, B. (1974). Seismic velocities in dry and saturated cracked solids. *Journal of Geophysical Research*, *79*(35), 5412–5426. https://doi.org/10.1029/JB079i035p05412

Pennacchioni, G., Di Toro, G., Brack, P., Menegon, L., & Villa, I. M. (2006). Brittle–ductile–brittle deformation during cooling of tonalite (Adamello, Southern Italian Alps). *Tectonophysics*, *427*(1-4), 171–197. https://doi.org/10.1016/j.tecto.2006.05.019

Rempe, M., Mitchell, T., Renner, J., Nippress, S., Ben-Zion, Y., & Rockwell, T. (2013). Damage and seismic velocity structure of pulverized rocks near the San Andreas Fault. *Journal of Geophysical Research: Solid Earth*, *118*, 2813–2831. https://doi.org/10.1002/jgrb.50184

Renner, J., Hettkamp, T., & Rummel, F. (2000). Rock mechanical characterization of an argillaceous host rock of a potential radioactive waste repository. *Rock Mechanics and Rock Engineering*, *33*(3), 153–178. https://doi.org/10.1007/s006030070005

Rice, J. R. (1992). Fault stress states, pore pressure distributions, and the weakness of the San Andreas Fault. *International Geophysics*, *51*, 475–503. https://doi.org/10.1016/S0074-6142(08)62835-1

Sayers, C., & Kachanov, M. (1995). Microcrack-induced elastic wave anisotropy of brittle rocks. *Journal of Geophysical Research*, *100*(B3), 4149–4156. https://doi.org/10.1029/94JB03134

Schaff, D. P., & Beroza, G. C. (2004). Coseismic and postseismic velocity changes measured by repeating earthquakes. *Journal of Geophysical Research*, *109*, B103002. https://doi.org/10.1029/2004JB003011

Scholz, C., Dawers, N., Yu, J. Z., Anders, M., & Cowie, P. (1993). Fault growth and fault scaling laws: Preliminary results. *Journal of Geophysical Research*, *98*(B12), 21,951–21,961. https://doi.org/10.1029/93JB01008

Schubnel, A., Nishizawa, O., Masuda, K., Lei, X., Xue, Z., & Guéguen, Y. (2003). Velocity measurements and crack density determination during wet triaxial experiments on Oshima and Toki granites. *Thermo-Hydro-Mechanical Coupling in Fractured Rock*, 869–887. https://doi.org/10.1007/978-3-0348-8083-1_5

Schubnel, P. M. B., Thompson, B. D., Hazzard, J. F., & Young, R. P. (2006). Quantifying damage, saturation and anisotropy in cracked rocks by inverting elastic wave velocities. *Pure and Applied Geophysics*, *163*(5–6), 947–973. https://doi.org/10.1007/s00024-006-0061-y

Sevostianov, I., & Kachanov, M. (2009). Connections between elastic and conductive properties of heterogeneous materials. In *Advances in applied mechanics*, edited, (pp. 69–252). Amsterdam: Elsevier.

Smith, D. L., & Evans, B. (1984). Diffusional crack healing in quartz. *Journal of Geophysical Research*, *89*(B6), 4125–4135. https://doi.org/10.1029/JB089iB06p04125

Smith, S. A. F., Bistacchi, A., Mitchell, T. M., Mittempergher, S., & Di Toro, G. (2013). The structure of an exhumed intraplate seismogenic fault in crystalline basement. *Tectonophysics*, *599*, 29–44. https://doi.org/10.1016/j.tecto.2013.03.031

Song, I., & Renner, J. (2008). Hydromechanical properties of Fontainebleau sandstone: Experimental determination and micromechanical modeling. *Journal of Geophysical Research*, *113*, B09211. https://doi.org/10.1029/2007JB005055

Sotin, C., & Poirier, J. (1984). Analysis of high-temperature creep experiments by generalized nonlinear inversion. *Mechanics of Materials*, *3*(4), 311–317. https://doi.org/10.1016/0167-6636(84)90031-0

Sprunt, E. S., & Nur, A. (1979). Microcracking and healing in granites: New evidence from cathodoluminescence. *Science*, *205*(4405), 495–497. https://doi.org/10.1126/science.205.4405.495

Stewart, C., Lubinski, A., & Blenkarn, K. (1961). The use of alternating flow to characterize porous media having storage pores. *Journal of Petroleum Technology*, *13*(04), 383–389. https://doi.org/10.2118/1650-G-PA

Stierman, D. J. (1984). Geophysical and geological evidence for fracturing, water circulation and chemical alteration in granitic rocks adjacent to major strike-slip faults. *Journal of Geophysical Research*, *89*(B7), 5849–5857. https://doi.org/10.1029/JB089iB07p05849

Tadokoro, K., & Ando, M. (2002). Evidence for rapid fault healing derived from temporal changes in S wave splitting. *Geophysical Research Letters*, *29*(4), 1047. https://doi.org/10.1029/2001GL013644

Tenthorey, E., & Fitz Gerald, J. D. (2006). Feedbacks between deformation, hydrothermal reaction and permeability evolution in the crust: Experimental insights. *Earth and Planetary Science Letters*, *247*(1-2), 117–129. https://doi.org/10.1016/j.epsl.2006.05.005

Terzaghi, R. D. (1965). Sources of error in joint surveys. *Geotechnique*, *15*(3), 287–304. https://doi.org/10.1680/geot.1965.15.3.287

Townend, J., & Zoback, M. D. (2000). How faulting keeps the crust strong. *Geology*, *28*(5), 399–402. https://doi.org/10.1130/0091-7613(2000)28<399:HFKTCS>2.0.CO;2

Vermilye, J. M., & Scholz, C. H. (1998). The process zone: A microstructural view of fault growth. *Journal of Geophysical Research*, *103*(B6), 12,223–12,237. https://doi.org/10.1029/98JB00957

Vinciguerra, S., Trovato, C., Meredith, P. G., Benson, P. M., Troise, C., & Natale, G. D. (2006). Understanding the seismic velocity structure of Campi Flegrei Caldera (Italy): From the laboratory to the field scale. *Pure and Applied Geophysics*, *163*(10), 2,205–2,221. https://doi.org/10.1007/s00024-006-0118-y

Wibberley, C. A., & Shimamoto, T. (2003). Internal structure and permeability of major strike-slip fault zones: The median tectonic line in Mie Prefecture, Southwest Japan. *Journal of Structural Geology*, *25*(1), 59–78. https://doi.org/10.1016/S0191-8141(02)00014-7

Zhao, D., Kanamori, H., Negishi, H., & Wiens, D. (1996). Tomography of the source area of the 1995 Kobe earthquake: Evidence for fluids at the hypocenter? *Science*, *274*(5294), 1891–1894. https://doi.org/10.1126/science.274.5294.1891

Zimmerman, R. (1984). Elastic moduli of a solid with spherical pores: New self-consistent method, paper presented at International Journal of Rock Mechanics and Mining Sciences & Geomechanics Abstracts, Elsevier.